TÉCNICO LISBOA

The influence of geostrophic flow and topography in Portugal's coastal upwelling

António Schiappa Pietra Vilela Lúcio

Thesis to obtain the Master of Science Degree in

Mechanical Engineering

Supervisors: Prof. Aires José Pinto dos Santos
Dr. Francisco Javier Campuzano Guillén

Examination Committee

Chairperson: Prof. Edgar Caetano Fernandes
Supervisor: Prof. Aires José Pinto dos Santos
Member of the Committee: Dr. Paulo Nogueira Brás de Oliveira

October 2020

Acknowledgments

I dedicate the first words to Professor Aires dos Santos, who, perhaps inadvertently and throughout all of his lectures, instilled in me the beauty of rigour. His constant pursuit for clear and simple reasoning, but also good-looking aesthetics and careful mathematical derivations were most definitely inspiring. Always present to clear up any doubts, and with great suggestions, it was above all an enormous pleasure to have worked with him.

Secondly, I thank researcher Francisco Campuzano for having provided many suggestions and files that were essential for this thesis.

To all my family, especially my mother and my father, thank you for your everlasting support.

Henrique, Miguel and Mariana, the moments spent with you were vital. I am most grateful to have you as friends.

Resumo

Esta tese apresenta a influência da corrente geostrófica e da batimetria para duas localizações no Norte e no Sul de Portugal.

Usando uma extensão do modelo de Ekman feita por Estrade et al. (2008), obteve-se uma função de corrente que depende, entre outras variáveis, da tensão de corte, da corrente geostrófica zonal e também da batimetria da latitude a estudar. A escassez de dados, usual junto à costa, obrigou a uma interpolação de vários parâmetros.

Para calcular os índices de afloramento de acordo com a formulação de Marchesiello and Estrade (2010), foram calculadas velocidades verticais. Estas são obtidas por diferenciação da função de corrente em ordem a x, a coordenada que define a direcção zonal.

Juntamente com o tradicional índice de *upwelling* de Bakun e um índice baseado na temperatura do mar, verificou-se que a batimetria, embora mude a intensidade das velocidades verticais, não teve grande impacto na estrutura do afloramento costeiro entre o Norte e o Sul. A corrente geostrófica para a costa, por outro lado, impediu as normais condições de afloramento no Sul em alguns meses da análise. No Norte o efeito foi o oposto, havendo uma intensificação do afloramento.

Palavras-chave: afloramento costeiro, oceano pouco profundo, plataforma interior, geostrofia, batimetria

Abstract

The present study evaluates the influence of geostrophic flow and bathymetry for two locations in the North and South of Portugal.

Using an extension of Ekman's theory done by Estrade et al. (2008), a stream function is computed. Due to the scarcity of shear stress and geostrophic surface current data in the nearshore region, interpolation had to be performed.

Vertical velocities were obtained by differentiating the stream function in order to the offshore distance x. These are used to calculate a dynamical index using Marchesiello and Estrade (2010) formulation.

Together with a traditional Bakun and SST upwelling indices, it was found that even though bathymetry influences the intensity of vertical velocities, its impact on upwelling structure is not large. Geostrophic onshore flow, on the other hand, was found to hinder upwelling conditions in the South, whilst enhancing them in the North.

Keywords: coastal upwelling, inner shelf, shallow sea, geostrophy, bathymetry

Contents

List of Figures

Nomenclature

Acronyms

AC	Azores Current
AH	Azores High
CIUE	Canary Islands Upwelling Ecossystem
CUI	Coastal Upwelling Index
CUI–L_E	Coastal Upwelling Index based on L_E
DFI	Depth of Frictional Influence
ECUI	Ekman Coastal Upwelling Index
EUMOFA	European Market Observatory for Fisheries and Aquaculture
IBL	Iberian Thermal Low
IL	Icelandic Low
IP	Iberian Peninsula
IPC	Iberian Poleward Current
IPSU	Iberian Poleward Slope Undercurrent
JEBAR	Joint Effect of Baroclinicity and Relief
MABL	Marine Atmospheric Boundary Layer
MEDDIES	Mediterranean Water Eddies
NAC	North Atlantic Current
NAO	North Altantic Oscillation
NH	Northern Hemisphere
PoC	Portugal Current
SH	Southern Hemisphere
SST	Sea Surface Temperature
SST–I	Sea Surface Temperature Upwelling Index
SWODDIES	Slope Water Oceanic Eddies
TKE	Turbulent Kinetic Energy
UI	Upwelling Index
UIA	Upwelling Index Anomaly
WIBP	Western Iberia Buoyant Plume
WIUE	Western Iberia Upwelling Ecossystem

Greek symbols

γ	upwelling restoring time-scale
μ	molecular viscosity coefficient
ρ_0	reference density
τ	shear stress

Roman symbols

f	Coriolis parameter
h	bottom depth
K	eddy viscosity coefficient
p	pressure
T	temperature
x, y, z	eastward, northward, and upward directions
x_n	cross-shore coordinate in the Marchesiello and Estrade (2010) article
u, v, w	velocities in the eastward, northward and upward directions

Subscripts

A	alongshore component
B	subsurface
E	Ekman component/Ekman related
g	geostrophic component
H	horizontal component
N	North location: $40.50\,^\circ\mathrm{N}$
O	offshore
S	South location: $37.75\,^\circ\mathrm{N}$
V	vertical component

Superscripts

s	surface component

Chapter 1

Introduction

1.1 Context

Coastal upwelling has long been known as the main reason why the Portuguese coast is so rich in fish. The ascent of cold and nutrient-packed waters from great depths allows phytoplankton — the main pillar of the food chain — to thrive. Fish, of course, are an important link of the chain and remain one of the most crucial elements of the Portuguese diet. Actually, Portugal is the most relevant country in the EU in terms of per capita fish consumption, according to the 2019 EUMOFA report. From an economical perspective, a weak upwelling season can be a struggle for the fishing industry, as Portugal is not only a great consumer, but a great exporter of quality fish: fresh and canned.

Over the years, upwelling has caught the interest of many researchers due to its mathematical challenges, but also due to its practical applications. The present thesis sways towards the theoretical and mathematical aspects of upwelling.

Bathymetry, particularly, is an important facet to take into consideration when characterizing a coastal region. Broad continental shelves, unlike the narrow ones, allow upwelling separation from the coast, thereby providing a larvae retention mechanism which, in addition to coastal upwelling, is paramount for their survival and successful reproduction of fish.

1.2 Objectives

- Using an analytical model, find eventual differences in the upwelling structure due to bathymetry between the North and South of Portugal;

- Assess the importance of bathymetry and zonal geostrophic flow in the upwelling indices for both locations.

1.3 Thesis Outline

Chapter 1 defines the thesis' objectives and introduces the upwelling topic.

Chapter 2 presents the state of the art. Classical aspects of the Ekman upwelling, specific atmospheric and oceanic topics phenomena known to the IP and the main theme, upwelling in shallow waters, are addressed.

In **Chapter 3**, results from other papers are reproduced for the study location. Differences in u, v, and w velocities using the analytical model for both locations are presented. Upwelling index calculation is done for both bathymetries.
In **Chapter 4** the results are discussed and possible error sources are evaluated.
Chapter 5 addresses the major achievements of this study and ideas for future work.

Chapter 2

Literature Review

2.1 Study location

Two latitudes will be studied in this thesis: $37.75\,^{\circ}\,\mathrm{N}$ and $40.50\,^{\circ}\,\mathrm{N}$. They're both located inside the WIUE ($37^{\circ}\,\mathrm{N}$–$44^{\circ}\,\mathrm{N}$), which is a sub-region of the larger CIUE. In the offshore region of the former ecosystem, various currents of different dimensions, transport, and localization are important. Specifically, the PoC, the IPC and the IPSU.

According to Mason et al. (2006) report, the PoC is a broad current ($10^{\circ}\,\mathrm{W}$–$24^{\circ}\,\mathrm{W}$) which flows predominantly southward, allowing communication of two important currents, the NAC and the AC . The IPC and IPSU are both counter-currents which develop along the shelf slope and can be detected year-round, however, in the winter, the IPC reaches its maximum intensity whilst the IPSU reaches its lowest. Forcing mechanisms for these currents are still debated. Teles-Machado et al. (2016a) say that during June, July and August, besides other effects like wind slope induced torque, JEBAR remains dominant. Regarding their vertical location, it is known that the IPC is contained within the surface and $z \approx 350\,\mathrm{m}$, whereas the IPSU sits between $z \approx 600\,\mathrm{m}$ and $z \approx 1200\,\mathrm{m}$.

2.2 General concepts

In the NH, coastal upwelling is the rise of deep waters in response to an equatorward/southward wind. To understand how this happens one must study the work of Ekman (1905). His study relies on a series of assumptions: steady state; infinite ocean; uniform horizontal distribution of wind; constant density; constant Coriolis parameter; horizontal free surface (for a given depth the horizontal pressure gradient is nil); constant vertical turbulent viscosity; non-existing horizontal turbulence viscosity and, finally, the ocean is modelled as a series of horizontal and sequential layers.

The main conclusion of the article is the following: the combined effect of friction and Coriolis forces generates a surface current that is deflected 45° *cum sole* relatively to the wind's original direction. With increasing depth, the viscosity starts acting and the absolute value of the velocity vector diminishes at

the same time it rotates clockwise (for the NH). Graphically, these two effects lead to the famous Ekman spiral. The depth at which the velocity vector in the ocean makes $180°$ with the wind velocity vector at the surface is called the DFI. The array of depths between the surface and the DFI is called the Ekman layer. The average movement of the Ekman layer is the Ekman transport. All these results are represented in **Figure 2.1**.

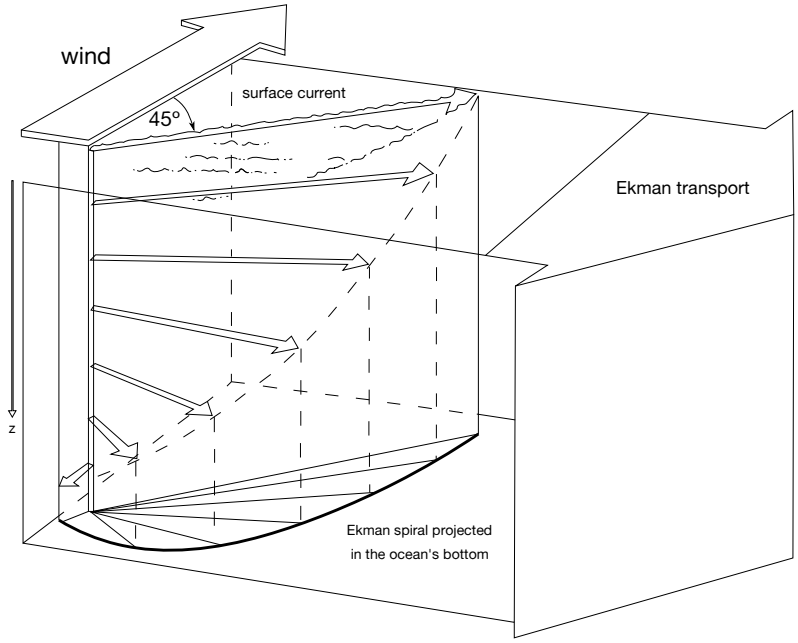

Figure 2.1: Ekman spiral in the NH – after Trujillo and Thurman (2017)

The mass balance tells us that the westward flow has to be compensated by an onshore flow at depth coupled with rise of water. Hence, the connexion is done: an equator-ward wind generates upwelling.

Coastal upwelling situations can be checked with SST satellite images. Usually, with the rise of deep waters (which have lower temperatures than those at the surface) a tongue of "cold" water is observed near the coast. This temperature decrease can sometimes be enhanced at capes and promontories, as Peliz et al. (2002) say. It is important to notice that there is a lag between the effect of an upwelling favourable wind regime and the rise of "cold" waters.
Upwelling has a crucial role redistributing heat and salt along-slope, yet aside from that, it is also responsible for the transport of nutrients, larvae and other biological material, as stated in the report by Mason et al. (2006).

In his paper, Ekman considered an ocean with an horizontal free surface, but in reality that is not the case, so other dynamics should arise when said hypothesis is discarded. As a matter of fact, when superficial waters flow offshore, the free surface of the ocean rises offshore as well, sloping downwards towards the coast. In other words, a zonal pressure gradient appears. In Oceanography, it is standard to take an x axis that is positive towards East and an y axis that is positive towards North. Hence, as x increases, pressure decreases $(\partial p/\partial x < 0)$. Using the x-direction momentum equations for geostrophic flow:

$$-\frac{1}{\rho_0}\frac{\partial p}{\partial x} + f v_g = 0 \Leftrightarrow v_g = \frac{1}{\rho_0 f}\frac{\partial p}{\partial x} \tag{2.1}$$

A slope of the free surface ultimately creates an equator-ward current. For this reason, using the parallelogram law for vector addition, the resultant surface current has increased intensity, but makes a smaller angle with the wind vector, as seen in **Figure 2.2**.

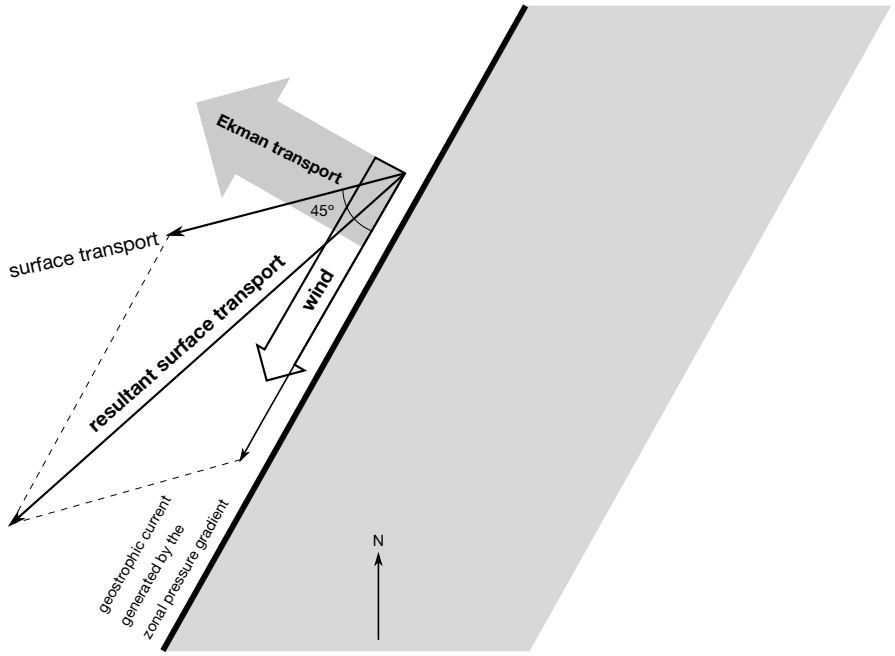

Figure 2.2: Ideal coastal upwelling situation in the NH, adapted from The Open University et al. (1989)

Actually, despite having a positive slope, the isobars tend to go horizontal as one gets deeper down the ocean. Past the level of no current, where the slope of the isobars is nil and there is no zonal movement of water, the slope gets negative and by **Equation 2.1** a poleward flow appears.

Until now, only one upwelling contribution has been mentioned — the Ekman transport — but in reality, as said in Capet et al. (2004), coastal upwelling has two contributions: Ekman transport and Ekman pumping (or suction). Ekman pumping happens if the shear stress considered in the Ekman transport calculation varies with position. To find a relationship between the Ekman pumping velocity and the shear stress at the surface, it is usual to start by integrating the continuity equation. Rearranging the Leibniz integral rule:

$$\int_a^b \frac{\partial f\left(x,z\right)}{\partial z} = \frac{\partial}{\partial z}\int_a^b f(x,z)dx - f\left(x,b\right)\frac{\partial b}{\partial z} + f\left(x,a\right)\frac{\partial a}{\partial z} \tag{2.2}$$

Using **Equation 2.2** to integrate the continuity equation (for incompressible flows) from the Ekman depth $z = \text{DFI} = D_E$ to the free surface $z = \eta$:

$$\begin{aligned}\int_{z=-D_E}^{z=\eta}\left(\frac{\partial u}{\partial x}+\frac{\partial v}{\partial y}+\frac{\partial w}{\partial z}\right)dz &= \int_{z=-D_E}^{z=\eta}\frac{\partial u}{\partial x}dz + \int_{z=-D_E}^{z=\eta}\frac{\partial v}{\partial y}dz + \int_{z=-D_E}^{z=\eta}\frac{\partial w}{\partial z}dz = \\ &= \frac{\partial}{\partial x}\int_{z=-D_E}^{z=\eta} u dz - \left(u\right)_{z=\eta}\frac{\partial \eta}{\partial x} + \left(u\right)_{z=-D_E}\frac{\partial\left(-D_E\right)}{\partial x} \\ &+ \frac{\partial}{\partial y}\int_{z=-D_E}^{z=\eta} v dz - \left(v\right)_{z=\eta}\frac{\partial \eta}{\partial y} + \left(v\right)_{z=-D_E}\frac{\partial\left(-D_E\right)}{\partial y} \\ &+ \left(w\right)_{z=\eta} - \left(w\right)_{z=-D_E} = 0\end{aligned} \tag{2.3}$$

Boundary conditions:

$$(w)_{z=\eta} = \frac{d\eta}{dt} = \frac{\partial \eta}{\partial t} + (u)_{z=\eta}\frac{\partial \eta}{\partial x} + (v)_{z=\eta}\frac{\partial \eta}{\partial y}$$

$$(w)_{z=-D_E} = \frac{d(-D_E)}{dt} = \frac{\partial(-D_E)}{\partial t} + (u)_{z=-D_E}\frac{\partial(-D_E)}{\partial x} + (v)_{z=-D_E}\frac{\partial(-D_E)}{\partial y}$$

The kinematic conditions refer to the vertical velocity at the surface (which has to be null, otherwise the surface would go up into the air) and the total vertical velocity at the lower boundary of the top Ekman layer. By definition, Ekman velocities are zero at the bottom of the top Ekman layer (also known as mixing layer). Furthermore, while the divergence is not compensated by a convergence, $\frac{\partial D_E}{\partial t} \approx 0$. Applying these simplifications, various terms cancel out and one arrives to:

$$(w_E)_0 = \frac{\partial \eta}{\partial t} = -\frac{\partial}{\partial x}\int_{z=-D_E}^{z=\eta} u dz - \frac{\partial}{\partial y}\int_{z=-D_E}^{z=\eta} v dz = -\frac{\partial S_x}{\partial x} - \frac{\partial S_y}{\partial y} = -\nabla_h \cdot \vec{S} \tag{2.4}$$

Where $\vec{S}$ is a common notation for the surface Ekman transport vector. Let us now consider the momentum equations for a steady and barotropic flow with low Rossby number.

$$-fv = -\frac{1}{\rho_0}\frac{\partial p}{\partial x} + \frac{1}{\rho_0}\frac{\partial \tau_{zx}}{\partial z} \quad , \quad fu = -\frac{1}{\rho_0}\frac{\partial p}{\partial y} + \frac{1}{\rho_0}\frac{\partial \tau_{zy}}{\partial z} \tag{2.5}$$

Knowing Ekman's assumptions, the previous equations reduce to:

$$\frac{1}{\rho_0}\frac{\partial \tau_{zx}}{\partial z} = -fv_E \quad , \quad \frac{1}{\rho_0}\frac{\partial \tau_{zy}}{\partial z} = fu_E \tag{2.6}$$

Integrating them in the vertical direction, one has:

$$\frac{1}{\rho_0}\int_{z=-D_E}^{z=\eta}\frac{\partial \tau_{zy}}{\partial z}dz = f\int_{z=-D_E}^{z=\eta} u_E dz \Leftrightarrow \frac{1}{\rho_0}\tau^s_{zy} = -fS_x \Leftrightarrow S_x = \frac{\tau^s_{zy}}{\rho_0 f} \tag{2.7a}$$

$$\frac{1}{\rho_0}\int_{z=-D_E}^{z=\eta}\frac{\partial \tau_{zx}}{\partial z}dz = -f\int_{z=-D_E}^{z=\eta} v_E dz \Leftrightarrow \frac{1}{\rho_0}\tau^s_{zx} = -fS_y \Leftrightarrow S_y = -\frac{\tau^s_{zx}}{\rho_0 f} \tag{2.7b}$$

In the above equations, τ^s_{zy} and τ^s_{zx} denote the meridional and zonal components of the wind shear stress at the surface of the ocean. Plugging this into (2.4):

$$\begin{aligned} -\nabla_h \cdot \left(\frac{\tau^s_{zy}}{\rho_0 f}, -\frac{\tau^s_{zx}}{\rho_0 f}\right) &= -\left(\frac{\partial}{\partial x}, \frac{\partial}{\partial y}\right)\cdot\left(\frac{\tau^s_{zy}}{\rho_0 f}, -\frac{\tau^s_{zx}}{\rho_0 f}\right) \\ &= -\left[\frac{\partial}{\partial x}\left(\frac{\tau^s_{zy}}{\rho_0 f}\right) - \frac{\partial}{\partial y}\left(\frac{\tau^s_{zx}}{\rho_0 f}\right)\right] = -\left[\nabla \times \left(\frac{\vec{\tau}^s}{\rho_0 f}\right)\right]_z \end{aligned} \tag{2.8}$$

The beta ($\beta = \partial f/\partial y$) effect contribution $\frac{\beta \tau_{zx}}{\rho_0 f^2}$ is zero if $f = \text{const}$, which is assumed to be the case.

$$(w_E)_0 = -\frac{1}{\rho_0 f}(\nabla \times \vec{\tau}^s)_z \tag{2.9}$$

As stated in the book by Stewart (2012), this is the vertical Ekman velocity at the top of the layer. But, since the total vertical velocity must be zero at the surface, a balancing current has to appear:

$$(w_g)_0 = -(w_E)_0 \Rightarrow \boxed{(w_g)_0 = \nabla_h \cdot \vec{S} = \frac{1}{\rho_0 f}(\nabla \times \vec{\tau}^s)_z} \tag{2.10}$$

Conclusion: Ekman transport divergence is balanced by a convergence of the deep geostrophic flow.

For the Portuguese coast, zonal shear stress is of negligible contribution, whilst the meridional wind velocity distribution presents high zonal variability. Considering that it is usual for the shear stress (assuming it is more or less co-linear with the velocity distribution) to decrease towards the coast, looking at **Figure 2.3**, positive curl is generated (*i.e.* Ekman pumping). According to Capet et al. (2004), a strong wind drop-off near the coast promotes horizontally-distributed Ekman pumping. Conversely, if the wind is substantial nearshore, strong and localized coastal upwelling occurs. This last wind distribution is best at bringing deep parcels to the surface. The physics of the drop-off can be explained with boundary layer dynamics and friction forces at the sea-land surface.

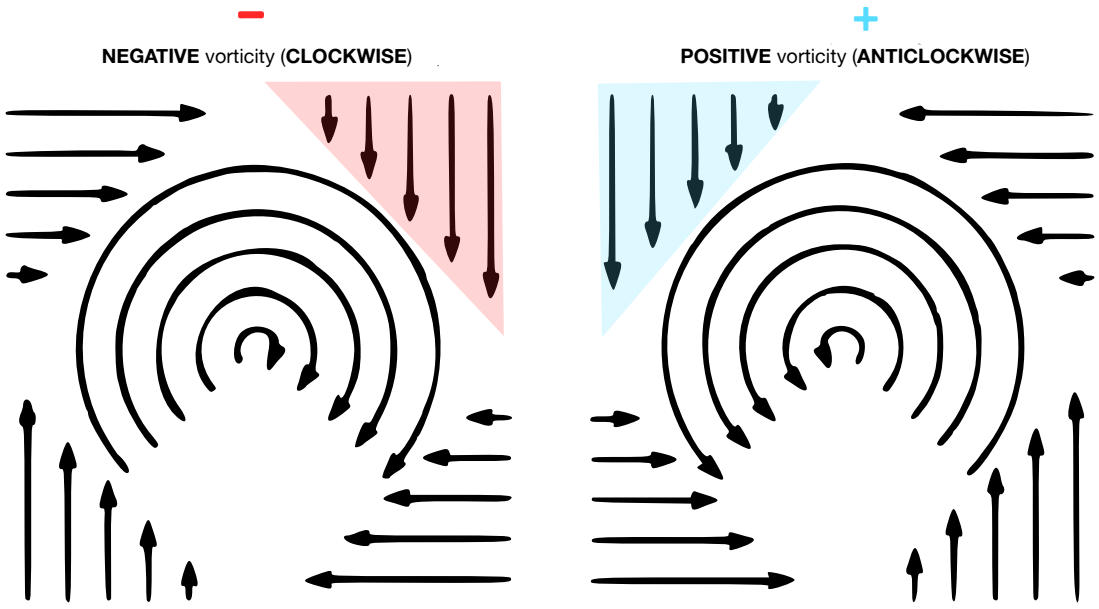

Figure 2.3: Different velocity distributions generate negative and positive vorticities, adapted from The Open University et al. (1989)

Having seen how the wind influences upwelling dynamics, it also of interest to examine the establishment of the wind regime itself. For the WIUE, the spatial arrangement of the Azores High and the Icelandic Low is of the utmost importance. This duo is, for the most part, responsible for the strong northerly winds that affect the coastal areas during Summer. As stated in Fiuza et al. (1982) paper, considering a climatological time-scale, the AH has a bigger influence on the wind profiles than the IL. Relvas et al. (2007) mention that during the summertime, the characteristic season for upwelling, the AH happens to be reinforced and slightly shifted towards the northern parts of the Portuguese territory, while the IL weakens at the same time. This configuration originates a strong northerly wind.

2.3 Mesoscale structures

The number of mesoscale structures is extensive. Filaments, eddies, jets, fronts, and internal waves are examples of these influential phenomena. Shallow waters present various types of fronts: shelf break fronts (coastal *vs.* open ocean waters), shallow sea fronts (tidal currents *vs.* stratification), and finally the upwelling front.

Upwelling fronts are formed when the thermocline reaches the ocean's surface as a result of the ascent of deep waters. The weakening and strengthening of the Ekman layer horizontal movement defines most of the front's position. The study of Shanks et al. (2000) shows how the surface convergence within the frontal region can conduce to a retention of larvae. **Figure 2.4** illustrates how the front appears in the ocean.

Internal waves are generated when the interface between layers of different densities is disturbed. Said waves, just like surface ones, ultimately brake. The breaking of internal waves promotes the mixing of waters with different densities, inducing turbulence in the ocean.

2.3.1 Filaments

Filaments have a major role in the exchange of coastal and offshore water masses. Relvas et al. (2007) conclude that their development can not be attributed to a single mechanism. Haynes et al. (1993) presents 3 of them: topographic forcing, baroclinic instabilities and geostrophical turbulence. A year before, Batteen et al. (1992) studied the influence of the wind stress curl in their formation. More recently, Peliz et al. (2002) proposed that flow interaction can be an essential part of their genesis. Be that as it may, it is incontestable that in the WIUE filaments are almost always anchored to some kind of cape or promontory. A great example of an SST satellite image that shows a distinct filament was presented in Peliz et al. (2002). The figure is reproduced in **Figure 2.6**.

Following Haynes et al. (1993) article, the development of filaments offshore of the IP starts with the typical cold water band aligned with the coastline. After sometime of its appearance, the band starts to become fringed, indicating the beginning of filament formation. Major filaments start to form in late July, being usual for them to reach maximum length in the end of September. After that, it is thought that with an unfavourable wind regime, the filaments stop generating.

2.3.2 Eddies

Eddies, as stated in Mason et al. (2006), have different dimensions ($10\,\mathrm{km}$ to $100\,\mathrm{km}$) and can be generated wherever there is a tendency for the flow to bend, for example at a cape. As shown in **Figure 2.5**, they can also be formed at the boundaries of coastal currents by baroclinic instabilities. For the WIUE, two particular types of eddies have been studied and named: MEDDIES and SWODDIES.

According to Richardson et al. (2000), MEDDIES are generated when salty and warm water from the Mediterranean Current separates at the important bathymetric regions like canyons. Richardson et al.

mention an average span of $0.7\,\mathrm{years}$ and a mean diameter of $100\,\mathrm{km}$. MEDDIES present a lens-like structure, rotating clockwise and drifting predominantly southward from the point of their formation, as noted by Mason et al. (2006).

SWODDIES exhibit anticyclonic or cyclonic rotation and originate from a separation of the IPC at northern Iberian capes. They often display a dipole arrangement, where an anticyclone is coupled with a cyclone. These eddies carry the current's warm and salty waters offshore. Near Iberia, they were first detected at the Bay of Biscay by Pingree and Le Cann (1992). More recently, there is evidence of their detachment in the Portuguese coast, as say Teles-Machado et al. (2016b). There is no evidence of SWODDY formation in summer as of now. According to Mason et al. (2006), SWODDIES may have life spans of up to $1\,\mathrm{year}$ and depths of $1000\,\mathrm{m}$.

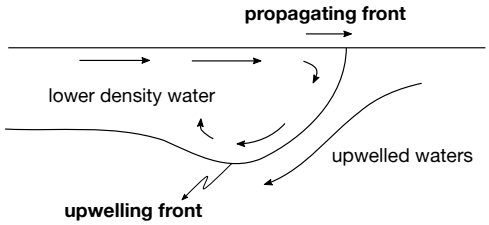

Figure 2.4: Scheme of an upwelling front propagating shoreward, after Shanks et al. (2000)

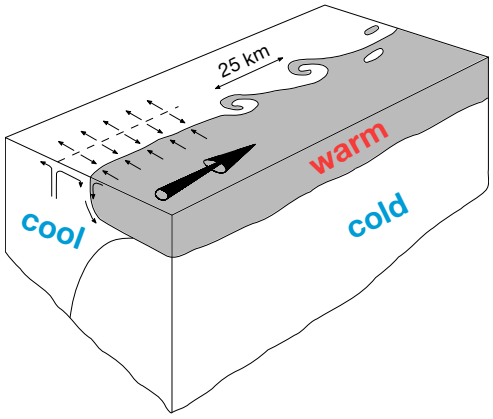

Figure 2.5: Scheme of shelf break front with associated eddies, after Simpson et al. (1981)

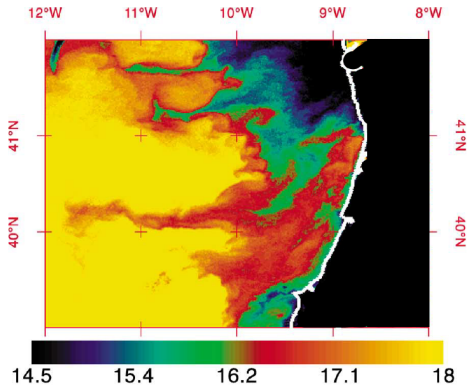

Figure 2.6: Brightness sea temperatures for $24/08/98$, after Peliz et al. (2002)

2.4 Upwelling interaction with other ocean phenomena

The article by Peliz et al. (2002) introduces the concept of WIBP. Briefly, this water plume of low salinity $(S < 35.8\,\mathrm{psu})$ originates from the various rivers that flow into the Atlantic Ocean at the northern part of the IP (Galician Rias, Lima, Minho, Douro, Mondego). It is present year-round, though it shrinks in the summer, when the river outflow decreases due to scarce precipitation.

As noted by Mason et al. (2006), this water lens accentuates stratification over the shelf which reduces the Ekman depth and therefore the Ekman transport. It is easy to understand why: since the stratification is stable (density decreases upwards), the buoyancy term of the TKE equation acts as a sink. The missing link is given by the mid 40s Prandtl's assumption that eddy viscosity depends on a velocity scale built with the square root of the TKE. The Ekman depth is related to eddy viscosity by:

$$\mathrm{DFI} \equiv D_E = \pi\sqrt{\frac{2K_V}{|f|}} \tag{2.11}$$

Reducing vertical eddy viscosity K_V (a function of the flow) leads to a smaller Ekman depth, reducing the Ekman transport.
As for the relation of WIBP with upwelling, Peliz et al. (2002) hypothesize that the water that feeds filaments can have its origin in the low salinity waters of the WIBP.

2.5 Atmosphere-Ocean Interaction

2.5.1 Iberian Thermal Low

During summertime, there is one influential atmospheric phenomenon in the IP that cannot be left unmentioned: the IBL. Briefly, this low pressure system develops over the central Iberian plateau and creates a anti-clockwise (convergent) movement at the surface which strengthens the already powerful northerly wind that prevails in Portugal's West Coast.

The study by Gaertner et al. (1993) describes this phenomenon in detail: the solar radiation heats the plateau; transferred heat is then convected back to the atmosphere by turbulence inducing a warming of its lower levels. Due to the temperature rise, there is a thermal expansion (molecules move faster and take up more space) and isobars shift upwards. A high pressure system (which is divergent and rotates clockwise) is created aloft. The divergence on the top is balanced by a convergence on the surface that originates a clockwise rotation, reinforcing the already strong northerly wind.

Figure 2.7 is a scheme of two ideal columns with the same amount of air molecules, therefore exerting the exact same pressure at the surface. It takes a shorter column of higher density to exert the same pressure as a taller, lower density one. Consequently, at an arbitrary reference level above the surface, the taller column will always exert a higher pressure than the shorter one. As a result, a pressure force develops above the surface.

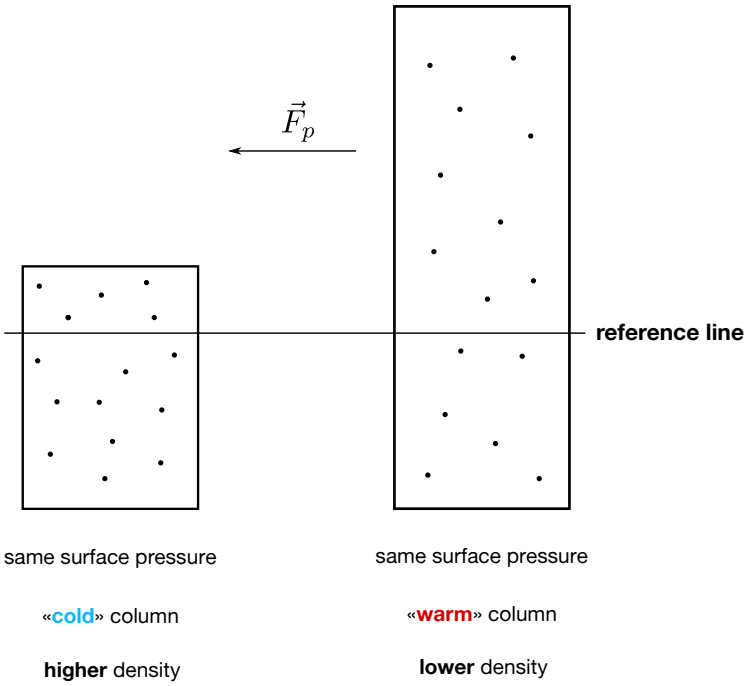

Figure 2.7: Pressure force generated at the top of the thermally expanded column

Looking at **Figure 2.8**, as the number of molecules above the isobar needs to be constant, it becomes clear why isobars need to move upwards when one moves closer to the thermally expanded column.

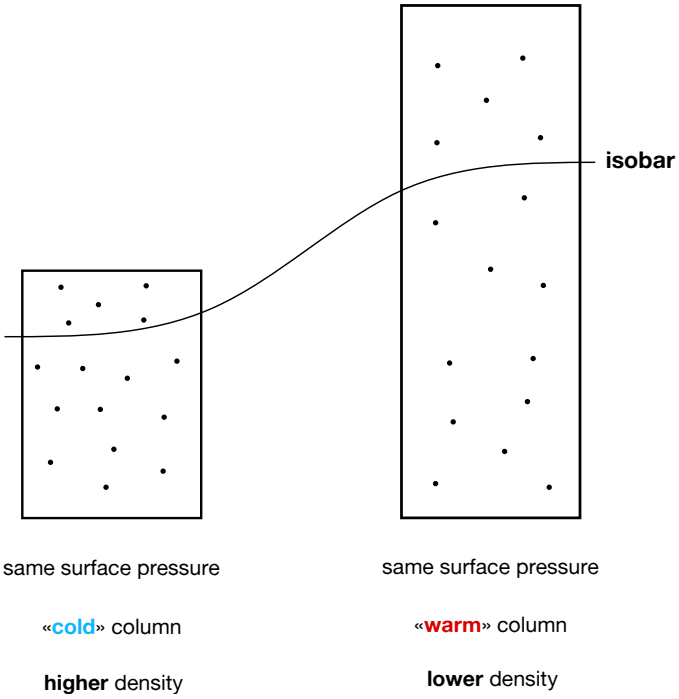

Figure 2.8: Shift of the isobars towards the expanded column of air

2.5.2 Expansion fans and compression bulges

Another important occurrence in the IP are expansion fans and compression bulges. They were first studied — in the context of Geophysics — by Winant et al. (1988). Expansion fans are regions in the MABL where a supercritical flow expands as a series of waves in response to a topographical feature, like a cape. Expansion fans happen downstream of capes, whereas compression bulges occur upstream. As explained in Monteiro et al. (2016), compression bulges are associated with a thickness increase and mean velocity decrease in the MABL. This implies that capes not only are important generating eddies and ocean flow perturbations, but also modifiers of the wind distribution, which is the main driving force of coastal upwelling.

2.5.3 SST-wind interaction, global warming impact on upwelling and atmospheric modes

In the article by Jin et al. (2009), the influence of SST in the wind distribution is studied. When SST variations induce temperature gradients (thus, density gradients) in the lower layers of the atmosphere, a vertical momentum gradient appears. The latter gradient implies a change in superficial wind shear. As previously stated, wind (or wind shear) distribution is the essential forcing mechanism of coastal upwelling. The conclusion is that SST variations change the MABL dynamics, which then affect the ocean in a feedback manner.

The similarity between the California upwelling system and the WIUE is long known. For instance, both systems share a thermal low that greatly affects the wind regime in coastal areas. Bakun (1990) studies a possible outcome of the intensification of the Californian thermal low due to global warming. The author says that an increase in the alongshore geostrophic wind can presumably lead to an increase in Ekman transport. However, only two years later, Bakun et al. (1992) verifies that an error in the measurements due to the tool that was used to capture the maritime wind can introduce wrong trends in the calculations. One cannot, therefore, state an upwelling increase due to global warming. This being said, it is true that alongshore geostrophic wind increases. More recently, Miranda et al. (2013), in a paper that tries to link climate change to upwelling, reinforce the idea of Bakun's 1990 article.

Another way to study the atmosphere's influence in the ocean is through teleconnection indices. A study by DeCastro et al. (2008) presents the importance of atmospheric indices in the WIUE. It was concluded that the UIA — defined as the deviation of the UI to its spatial and temporal average — can be explained with the East Atlantic pattern. The NAO was the second large scale mode with significant implications.

2.6 Shallow sea upwelling

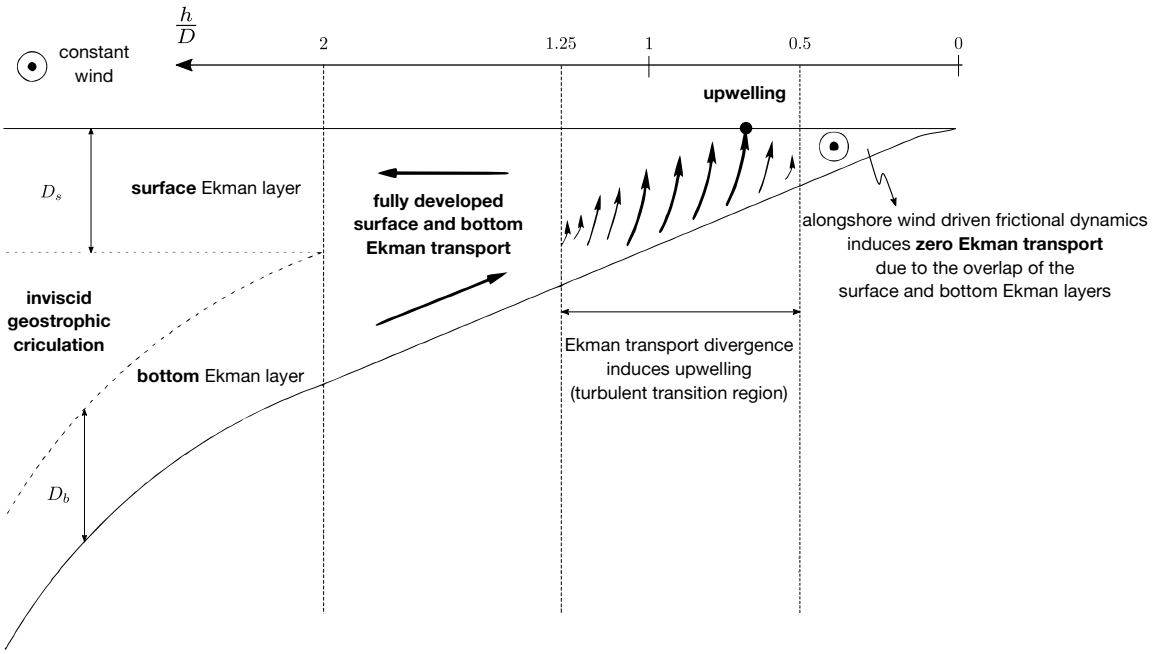

Figure 2.9: Conceptual scheme of the mechanism of upwelling separation from the coast – adapted from Estrade et al. (2008)

The study of upwelling in shallow seas initiates with the article of Welander (1957). A shallow sea is defined by DFI $\equiv D \approx h$, where h is the ocean's floor depth. In the said article, the unidimensional theory of Ekman is generalized into two dimensions. Welander begins with the steady state equations that describe the equilibrium between friction, Coriolis and pressure forces. After some algebraic manipulation, he arrives to a complex velocity and integrates it. From this last operation, horizontally-varying structure functions appear, see **Appendix A**. These functions are useful as they only depend on the ratio $\frac{h}{D}$ and ease interpretation of upcoming results.

2.6.1 Analytical model and conclusions of Estrade et al. (2008)

Using Welander's results, Estrade et al. (2008) explained why the upwelling cell centre separates from the coast. The authors studied the case of a semi-infinite ocean: finite in the zonal direction x and infinite in the meridional direction y.

The analytical model showed that, for alongshore winds, a critical isobath $h_c \approx 0.4D$ divides two flow regimes. One where friction forces dominate (bottom and top Ekman layers overlap; flow is parallel to the coastline) and the other, where Ekman transport diverges. As represented in **Figure 2.9**, until the critical isobath, there is no Ekman transport and thus, this region acts as a **kinematic barrier** to cross-shelf flow. Apart from an upwelling favourable wind, it is also noted that a broad shelf is a necessary condition for upwelling separation.

Here are some of the most relevant conclusions:

- analytical expression, adaptable to any bathymetry, for a stream function that allows representation of the upwelling cell using $\frac{h}{D}$ to describe the horizontal direction
- 90% of the Ekman transport occurs for $0.50 < \frac{h}{D} < 1.25$;
- an abrupt continental shelf favours an intense and narrow cell, whilst a broad shelf favours the contrary;
- the upwelling structure in the broad shelf is more sensitive to changes in Ekman depth;
- if the slope S is constant (linear bathymetry), then the zonal width of the upwelling cell is $0.75\frac{D}{S}$, see **Figure 2.10**.

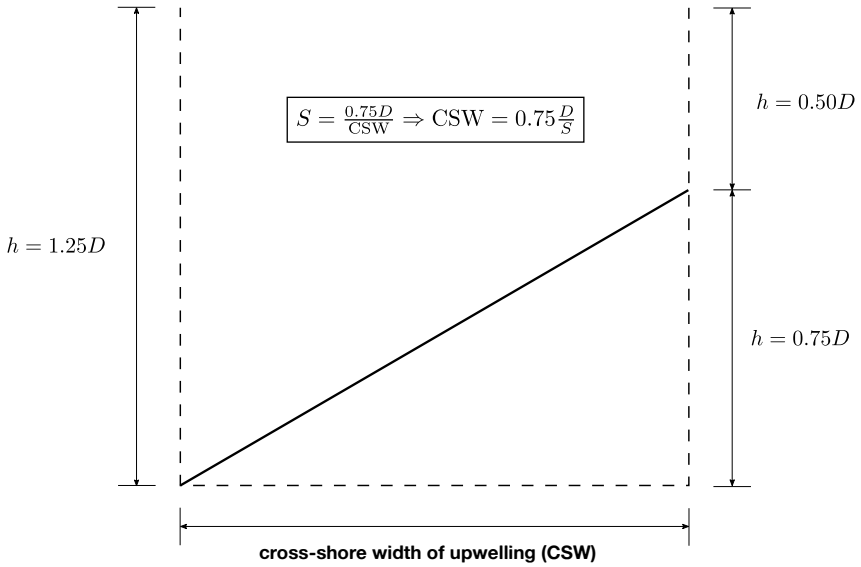

Figure 2.10: Linear bathymetry: the zonal width of the upwelling cell is $0.75D/S$

Despite the paper's focus on bathymetry, Estrade et al. also studied the influence of the cross-shore wind component, friction and stratification.

The cross-shore wind can be an input to the analytical model through τ_x. The authors found that with an offshore (onshore) wind, the Ekman transport is more (less) concentrated at the surface. Besides that, the upwelling separation is favoured by onshore winds and weakened by offshore ones.

Regarding friction, the authors concluded that, near the coast, despite an increase of the alongshore flow, the cross-shore flow remained almost zero. That means the upwelling cell more or less maintains its location and intensity, validating the constant viscosity hypothesis. It is worth mentioning that a depth-changing viscosity implies a variable Ekman depth. Thus, the analytical solution for the differential equation that governs the model has to be derived again.

Stratification was found to have an influence on the upwelling cell location: the cell oscillated between a nearshore and offshore position. Two phases are comprised in one oscillation: the outcropping phase and the layers splitting phase.

Outcropping phase: dense waters move shoreward; a density front forms and separates the inner stable shelf from the outer one; kinematic barrier and cell move offshore.
Layers splitting phase: isopycnal dome is generated and advected shoreward; bottom and top mixing layers separate; cell migrates shoreward

Even though the kinematic barrier (and upwelling cell) oscillate across the slope, the structure of the cell remains roughly unaltered.

The article also mentions that the analytical model was tested for a zonally-varying wind profile $\partial\tau_y^s/\partial x \neq 0$. It was determined that the separation mechanism weakened as a result of the lower friction nearshore. The kinematic barrier is a region where bottom shear stress balances wind friction. Since the boundary of the kinematic barrier moves shoreward when wind friction diminishes, it can be inferred that wind intensity nearshore is related with the width of the kinematic barrier.

2.6.2 Marchesiello and Estrade (2010) extension of the analytical model to cases with geostrophic onshore flow

Alongside the Estrade et al. (2008) article, Marchesiello and Estrade (2010) is another relevant study of the upwelling phenomena in the inner shelf. This time, the researchers found that the addition of a geostrophic onshore flow greatly affects the upwelling structure. Moreover, after analysing the stream function sensitivity to the zonal geostrophic flow u_g, an attractive result came up: since the expression $\partial\psi/\partial u_g$ is independent of viscosity, wind, latitude, or slope, it is possible that the effect of u_g in the upwelling process is similar in other coastal upwelling regions of the World.

A new index which incorporates the influence of bathymetry and geostrophic currents is also presented. The new index (CUI) actually unfolds into two separate indices: CUI and CUI–L_E. These are distinct because they use different definitions of upwelling cross-shore width. One of them accounts for the type of bathymetry profile (CUI) and the other (CUI–L_E) does not. The cross-shore width is selected according to:

$$L_U = \max\left[0.75\frac{D}{S}\ ,\ L_E = \pi\sqrt{\frac{2K_H}{|f|}}\ \right] \tag{2.12}$$

Four indices were studied: **CUI**, **CUI–L_E**, **SST–I** and **ECUI**. The authors defined the indices as follows:

$$\text{CUI} = \left|\frac{\tau_A}{\rho_0 f L_U}\right| + \frac{1}{L_U}\int_{x_n=0}^{x_n=L_U}\left[\int_{z=z_0}^{z=0}\left(\frac{\partial u_g}{\partial x}+\frac{\partial v_g}{\partial y}\right)dz\right]dx_n \tag{2.13a}$$

$$\text{CUI–}L_E = \left|\frac{\tau_A}{\rho_0 f L_E}\right| + \frac{1}{L_E}\int_{x_n=0}^{x_n=L_E}\left[\int_{z=z_0}^{z=0}\left(\frac{\partial u_g}{\partial x}+\frac{\partial v_g}{\partial y}\right)dz\right]dx_n \tag{2.13b}$$

$$\text{SST–I} = \frac{T-T_O}{T-T_B}\frac{\triangle z}{\gamma} \tag{2.13c}$$

$$\text{ECUI} = \left|\frac{\tau_A}{\rho_0 f L_U}\right| \tag{2.13d}$$

Marchesiello and Estrade also present a simpler version of **Equation 2.13a**, which can be obtained if $\partial u_g/\partial x = \text{const}$ and $\partial v_g/\partial y = 0$. Specifically, if $\partial u_g/\partial x = \text{const} = -u_g/L_U$, the second parcel of **Equation 2.13a** becomes:

$$\frac{1}{L_U}\int_{x_n=0}^{x_n=L_U}\left[\int_{z=z_0}^{z=0}\left(\frac{\partial u_g}{\partial x}+\frac{\partial v_g}{\partial y}\right)dz\right]dx_n = \frac{1}{L_U}\left[-\frac{u_g}{L_U}\left(0-z_0\right)\right]L_U = \frac{u_g}{L_U}z_0 \tag{2.14}$$

It will be seen further on that $z_0 = -D/2$ is good approximation, hence, CUI can also be given by:

$$\text{CUI} \approx \left|\frac{\tau_A}{\rho f L_U}\right| - \frac{u_G D}{2L_U} \tag{2.15}$$

The indices in this thesis were calculated directly from the stream function, as it will be seen afterwards, thus avoiding the extra constraint of $\partial u_g/\partial x = \text{const}$.

The UI based on SST is usually dimensionless, but Marchesiello and Estrade used a unit scaling parameter $\triangle z/\gamma$. This parameter has dimensions of velocity and comes from the 1-D heat balance where the vertical convection is balanced by the horizontal diffusion:

$$w\frac{\partial T}{\partial z} = \alpha_H \frac{\partial^2 T}{\partial x^2} \tag{2.16}$$

If $\alpha_H \frac{\partial^2 T}{\partial x^2} \approx \alpha_H \frac{T-T_O}{\triangle x^2}$, then the last equation becomes:

$$\alpha_H \frac{\partial^2 T}{\partial x^2} \approx \frac{T-T_0}{\triangle x^2/\alpha_H} = \frac{T-T_0}{\gamma} \tag{2.17}$$

Furthermore, if $\frac{\partial T}{\partial z} \approx \frac{T-T_B}{\triangle z}$:

$$w\frac{\partial T}{\partial z} = \alpha_H \frac{\partial^2 T}{\partial x^2} \Leftrightarrow w\frac{T-T_B}{\triangle z} = \frac{T-T_O}{\gamma} \Rightarrow w = \text{SST}-\text{I} = \frac{T-T_O}{T-T_B}\frac{\triangle z}{\gamma} \tag{2.18}$$

The authors pointed out that CUI and SST−I present the highest level of correlation, while ECUI and SST−I show the lowest. Apart from this, the differences between ECUI and CUI were attributed to the geostrophic influence, not the bathymetry.

The difference between CUI and CUI$-L_E$ gives an importance of the bathymetry: for a broad shelf case, they have distinct values, whilst for a narrow one, they coincide. The explanation is simple: since the slope S is larger on a narrow shelf, D/S is small and **Equation 2.12** gives $L_U = L_E$, which means CUI = CUI$-L_E$. This is more or less true if D does not change too much. Marchesiello and Estrade state the Peru region as an exception: it is a broad shelf with a small value of D/S since D is unusually low.

Even in the absence of stratification and variable Ekman depth, interesting results were obtained. The paper contributes to a more complete UI definition, which accounts for the importance of bathymetry and onshore geostrophic flows (alongshore pressure gradients).

Chapter 3

Analytical model and results

3.1 Analytical model

To understand the following sections, the main equations of the model are presented. A careful derivation is done in **Appendix A**. The results below keep a parameter that varies with the Hemisphere, $\lambda = f/|f|$.

Assumptions: steady state ($\partial/\partial t = 0$); $\mathrm{Ro} \ll 1$ (negligible advection); $H/L \ll 1$ (typical ocean basin); barotropic ocean; $K_V = \mathrm{const}$; $2D$ ocean ($\partial/\partial y = 0$); $(K_H)_x \gg K_V$ or $(\mathrm{Ek}_H)_x \ll \mathrm{Ek}_V$

Equations of momentum

$$-\frac{1}{\rho_0}\frac{\partial p}{\partial x} + fv + K_V\frac{\partial^2 u}{\partial z^2} = 0 \tag{3.1a}$$

$$-\frac{1}{\rho_0}\frac{\partial p}{\partial y} - fu + K_V\frac{\partial^2 v}{\partial z^2} = 0 \tag{3.1b}$$

Ekman's drift current problem

$$\frac{\partial^2 \tilde{u}_E}{\partial z^2} - c^2\tilde{u}_E = 0 \tag{3.2}$$

Complex notation momentum equation

$$K_V\frac{\partial^2 \tilde{u}}{\partial z^2} - if\tilde{u} = \frac{1}{\rho_0}\frac{\partial \tilde{p}}{\partial n} \tag{3.3}$$

Boundary conditions

$$K_V\left(\frac{\partial \tilde{u}}{\partial z}\right)_{z=0} = \frac{1}{\rho_0}\tilde{\tau}^s \underset{\partial u_g/\partial z=0}{\Rightarrow} K_V\left(\frac{\partial \tilde{u}_E}{\partial z}\right)_{z=0} = \frac{1}{\rho_0}\tilde{\tau}^s \tag{3.4a}$$

$$(\tilde{u})_{z=-h} = 0 \Leftrightarrow (\tilde{u}_E + \tilde{u}_g)_{z=-h} = 0 \tag{3.4b}$$

Total horizontal flow field

$$\tilde{u} = \tilde{u}_0 \frac{\sinh[c(z+h)]}{\cosh[ch]} + \tilde{u}_g \left(1 - \frac{\cosh[cz]}{\cosh[ch]}\right) \tag{3.5}$$

Ekman component of the flow

$$\tilde{u}_E = \tilde{u}_0 \frac{\sinh[c(z+h)]}{\cosh[ch]} - \tilde{u}_g \frac{\cosh[cz]}{\cosh[ch]} \tag{3.6}$$

Horizontally-varying structure functions

$$\alpha = \left(\cosh\left[\frac{\pi}{D}h\right]\cos\left[\frac{\pi}{D}h\right]\right)^2 + \left(\sinh\left[\frac{\pi}{D}h\right]\sin\left[\frac{\pi}{D}h\right]\right)^2 \tag{3.7a}$$

$$S_1 = \cosh\left[\frac{\pi}{D}h\right]\cos\left[\frac{\pi}{D}h\right]\alpha^{-1} \tag{3.7b}$$

$$S_2 = \sinh\left[\frac{\pi}{D}h\right]\sin\left[\frac{\lambda\pi}{D}h\right]\alpha^{-1} \tag{3.7c}$$

$$T_1 = \cosh\left[\frac{\pi}{D}h\right]\sinh\left[\frac{\pi}{D}h\right]\alpha^{-1} \tag{3.7d}$$

$$T_2 = \cos\left[\frac{\pi}{D}h\right]\sin\left[\frac{\lambda\pi}{D}h\right]\alpha^{-1} \tag{3.7e}$$

Total Ekman transport

$$U_E = (1 - S_1)\frac{\tau_y}{\rho_0 f} + S_2\frac{\tau_x}{\rho_0 f} - \frac{D}{2\pi}\left[(\lambda T_1 - T_2)\, v_g + (T_1 + \lambda T_2)\, u_g\right] \tag{3.8a}$$

$$U_E = -u_g h \tag{3.8b}$$

Meridional geostrophic velocity

$$v_g = \frac{2\pi}{\rho_0 f D}\left[\frac{1 - S_1}{\lambda T_1 - T_2}\tau_y + \frac{S_2}{\lambda T_1 - T_2}\tau_x\right] - u_g\frac{T_1 + \lambda T_2 - 2\pi h/D}{\lambda T_1 - T_2} \tag{3.9}$$

Stream function

$$w = \frac{\partial \psi}{\partial x} \tag{3.10a}$$

$$u = -\frac{\partial \psi}{\partial z} \tag{3.10b}$$

$$\psi(x,z) = \mathfrak{Re}\left\{\frac{1}{c}\left[\tilde{u}_0\left(1 - \frac{\cosh[c(z+h)]}{\cosh[ch]}\right) + \tilde{u}_g\frac{\sinh[cz]}{\sinh[ch]}\right]\right\} - u_g z \tag{3.10c}$$

3.2 Linear bathymetry

In **Figure 3.1**, the two columns show the influence of onshore geostrophic flow for three parameters: upwelling intensity $\psi/|U_E|$, total along shore flow velocity v, and alongshore geostrophic flow component v_g.

For the upwelling intensity contours of **Figure 3.1**, **Equation A.50** derived in **Appendix A** was applied. Using a linear $h(x) = -x/1000$ profile and typical values of wind stress for an upwelling situation ($\tau_y \approx -0.1\,\mathrm{Pa}$) results in a clearly distinguishable kinematic barrier and theoretical upwelling cross width. As expected, the addition of u_g brings great modifications to the stream function's structure: a new cell with positive values appears at greater depths, while the surface one loses about 50% of its intensity, just as reported by Marchesiello and Estrade (2010).

The middle row shows the upwelling jet, which the analytical model does not represent quite correctly, since it extends too far offshore, according to Marchesiello and Estrade (2010). Onshore geostrophic flow generates a poleward current ($v > 0$) for $h/D > 1.5$, which is approximately the inner shelf limit. The explanation for the poleward current is quite straightforward: the onshore geostrophic current gives rise to an offshore bottom Ekman flow, because part of it is deviated downwards. Due to the Ekman spiral, this implies a poleward current.

The last row shows how **Equation A.45** changes with x. Or h/D, for that matter, since $h = h(x)$. Looking at **Equation A.45**, $v_g \neq 0$ even if $u_g = 0$. This said, it is important to show why the v contours and the v_g evolution in Figure 6 of Marchesiello and Estrade (2010) are symmetrical to the correspondent graphs of **Figure 3.1**.

The first thing to note is that the sign of τ_y for favourable upwelling conditions changes with the hemisphere: it is $\tau_y > 0$ in the SH and $\tau_y < 0$ in the NH. For the two hemispheres at an offshore distance $h/D \approx 2$, and using $u_g = 0 = \tau_y$, **Equations 3.11a** (NH) and **3.11b** (SH) show how the sign of v_g changes. To calculate v_g, **Equation A.45** was applied.

$$(v_g)_{h/D\approx 2} = \underbrace{\frac{2\pi}{\rho_0 f D}}_{>0} \underbrace{\left[\frac{1-S_1}{T_1-T_2}\right]}_{=1 \text{ at } h/D\approx 2} \overbrace{\tau_y}^{<0} < 0 \tag{3.11a}$$

$$(v_g)_{h/D\approx 2} = \underbrace{\frac{2\pi}{\rho_0 f D}}_{<0} \underbrace{\left[\frac{1-S_1}{-T_1-T_2}\right]}_{=-1 \text{ at } h/D\approx 2} \overbrace{\tau_y}^{>0} > 0 \tag{3.11b}$$

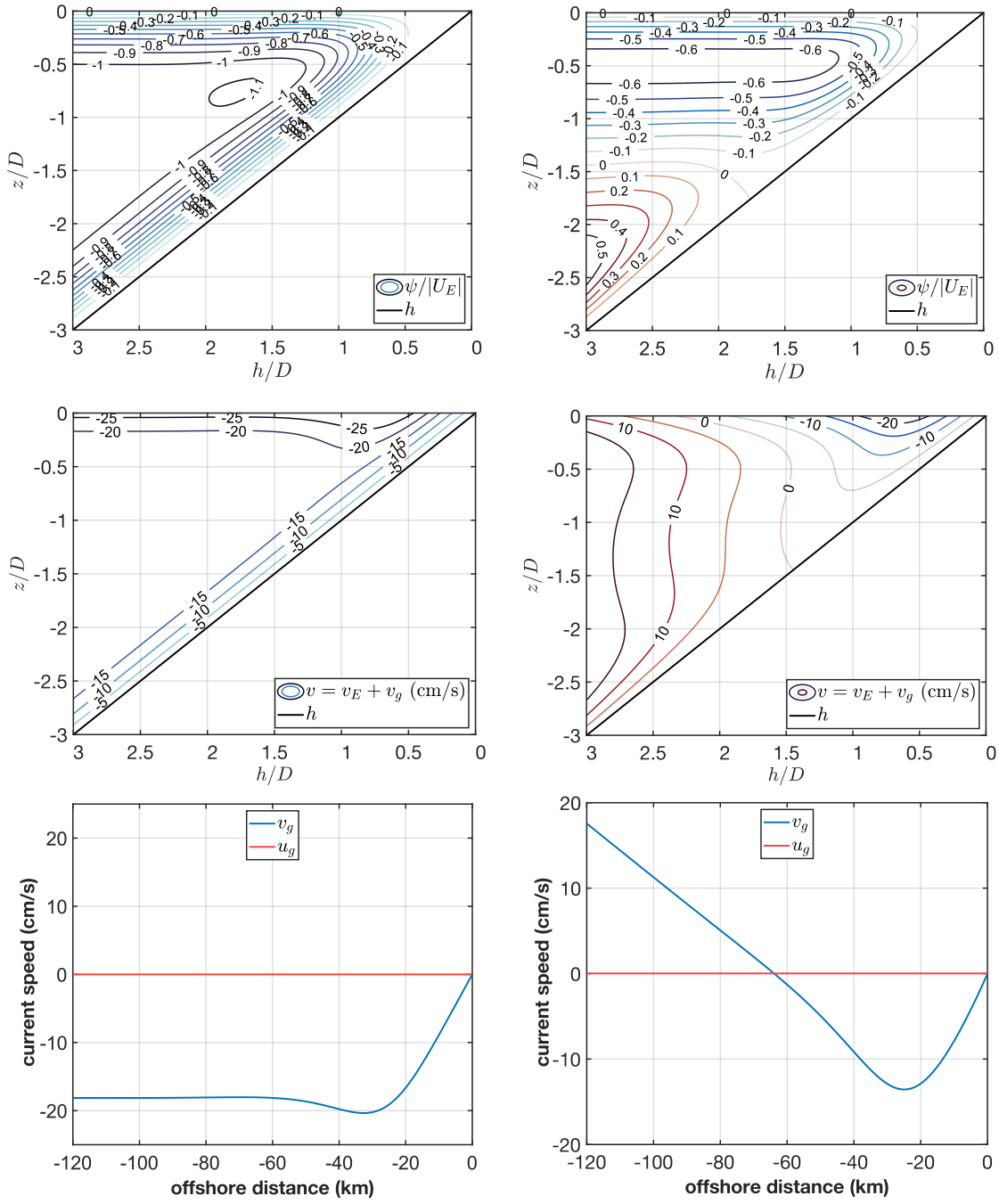

Figure 3.1: From top to bottom: upwelling intensity $\psi/|U_E|$, total along shore velocity v, and geostrophic flow. Left column: $u_g = 0\,\mathrm{m\,s^{-1}}$; Right column: $u_g = 0.02\,\mathrm{m\,s^{-1}}$

3.3 Real bathymetry

As the stream function can be applied to any kind of bathymetry, two latitudes were chosen for comparison. **Figure 3.2** shows how the Ekman depth influences the kinematic barrier and cell location, replicating results from Estrade et al. (2008) for the current thesis selected locations. The results are similar: the Ekman depth increase in the broad shelf originates a stronger displacement of the kinematic barrier, when compared to the narrow shelf. Despite some small variation, the upwelling cell in the South location is confined to the nearshore region.

Again, agreeing with Estrade's results, since the North location bathymetry does not rise monotonically, a two-cell structure can be seen for $D = 60\,\mathrm{m}$ and $D = 90\,\mathrm{m}$.

Additionally, **Figures 3.3** and **3.4** present the results with addition of an onshore and offshore geostrophic flow, respectively. The onshore flow agrees with the linear case quite nicely: the structure of the cell changes considerably for both locations and all D values.

The offshore geostrophic flow was not discussed in neither of Estrade or Marchesiello's papers. It is understandable that the offshore geostrophic flow case is not of great interest, after all it does not trigger such a different cell structure, yet its influence on the upwelling intensity values is of great importance. Actually, as it will be discussed in a further section, the nearshore monthly values of u_g for the North location are almost always negative.

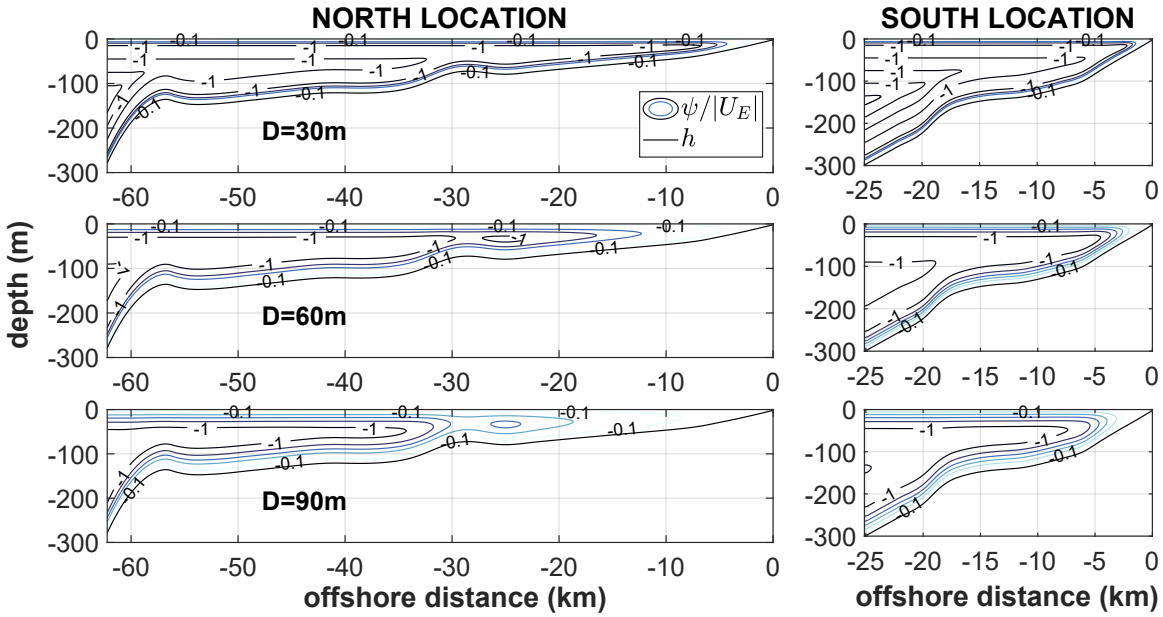

Figure 3.2: Upwelling intensity $\psi/\left|U_E\right|$ plotted over North and South locations with $u_g = 0\,\mathrm{m\,s^{-1}}$

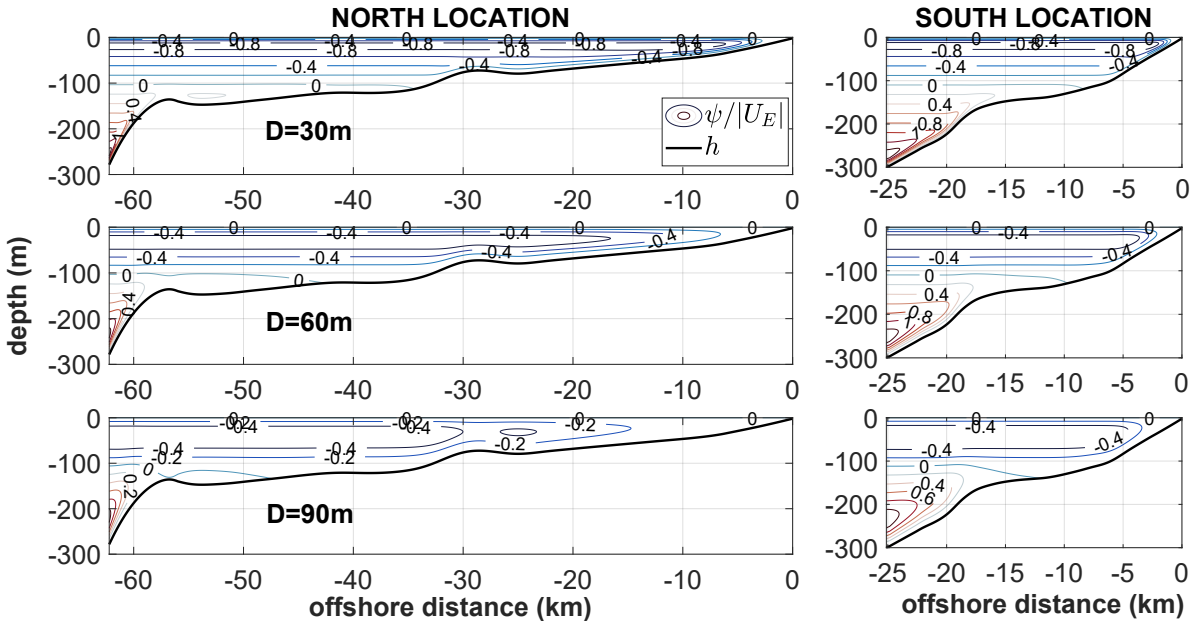

Figure 3.3: Upwelling intensity $\psi/\left|U_E\right|$ plotted over North and South locations with $u_g = 0.01\,\mathrm{m\,s^{-1}}$

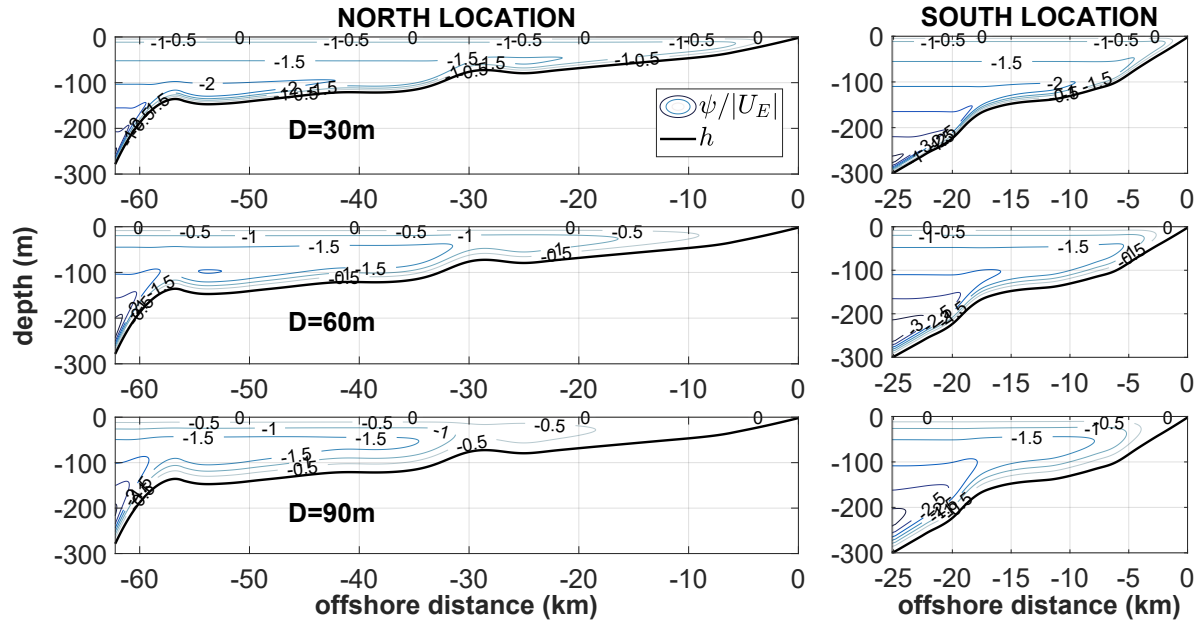

Figure 3.4: Upwelling intensity $\psi/\left|U_E\right|$ plotted over North and South locations with $u_g = -0.01\,\mathrm{m\,s^{-1}}$

Figure 3.5 shows the normalized cross-shore velocity and normalized stream function profiles with and without the influence of onshore geostrophic flow. The results do not depend on bathymetry, since they are taken for a specific offshore distance $h/D \approx 3.3$. At this location, the top and bottom Ekman layers are distinct and separated by a layer of inviscid geostrophic flow (recall **Figure 2.9**).

It is important to point out that in **Figure 8** by Marchesiello and Estrade (2010), it is not the cross-shore Ekman velocity u_E that is shown, but rather the full component u.

With **Equations A.18** and **A.29**, it can be shown that (for $z/D = 0$, $\tau_x = 0$):

$$\frac{u_E}{u_0} = \frac{\mathfrak{Re}\{\tilde{u}_E\}}{\mathfrak{Re}\{\tilde{u}_0\}} = T_1 - T_2 - u_0^{-1}\left(u_g S_1 - v_g S_2\right) \tag{3.12}$$

For $h/D \approx 3.3$, location where the graph is plotted, $T_1 - T_2 = 1$ and $S_1 = 0 = S_2$. Consequently, using **Equation 3.12**, for **both graphs**, the line of u_E/u_0 should start at -100, which does not happen, meaning that this is not the quantity being plotted. Furthermore, the absolute value of u_0 is needed in the denominator.

As referred by Marchesiello and Estrade (2010), the absolute value of the surface offshore transport is very close to the one of Ekman transport at $z = -D/2$.

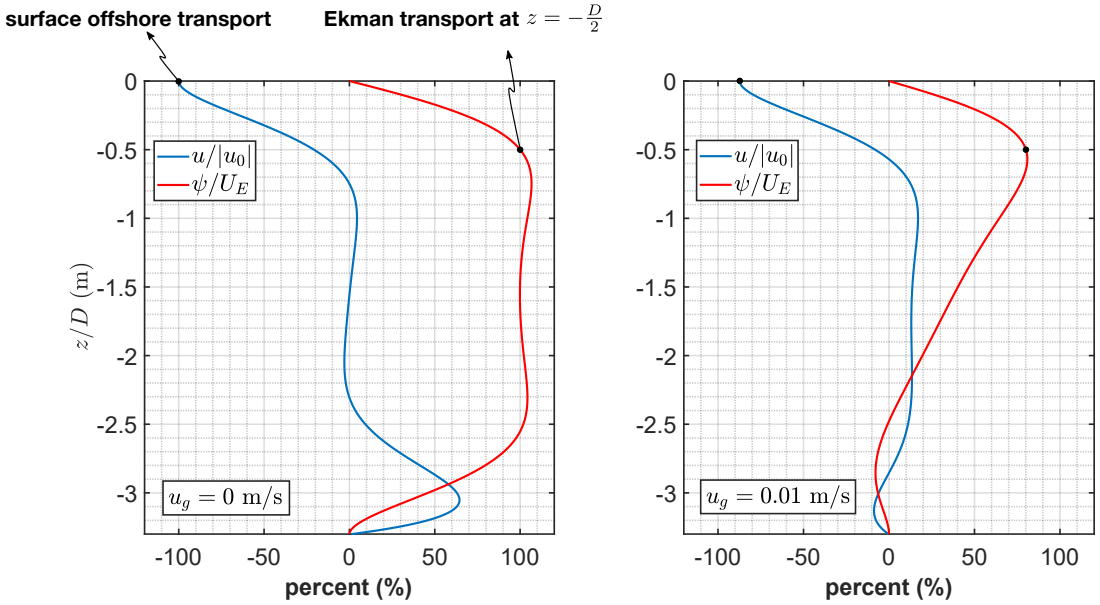

Figure 3.5: Cross-shore total velocity normalized by $|u_0|$ and stream function normalized by the Ekman transport U_E for $u_g = 0\,\mathrm{m\,s^{-1}}$ and $u_g = 0.01\,\mathrm{m\,s^{-1}}$

3.3.1 Velocity contours for North and South Locations

Figures 3.6 and **3.7** show the three velocities (u, v, and w) plotted over the smoothed North and South location bathymetries for two values of u_g and a constant shear stress $\tau_y = -0.01\,\mathrm{Pa}$. Note that the bathymetry was smoothed so it increases monotonically for both locations.

The results confirm that the upwelling separation is larger at $40.50\,^\circ\mathrm{N}$ than at $37.75\,^\circ\mathrm{N}$. At $40.50\,^\circ\mathrm{N}$, the boundary of the kinematic barrier appears at $x \approx -5\,\mathrm{km}$ for both values of u_g. For $37.75\,^\circ\mathrm{N}$, the boundary of the kinematic barrier appears at $x \approx -2.5\,\mathrm{km}$. The difference is not as staggering as the results from Estrade et al. (2008): the inner shelves of South Morocco (even broader) and Oregon (even narrower) explicit a larger difference for the same D. It can also be seen that, as a consequence of the steep slope, the vertical velocities are always higher at $37.75\,^\circ\mathrm{N}$.

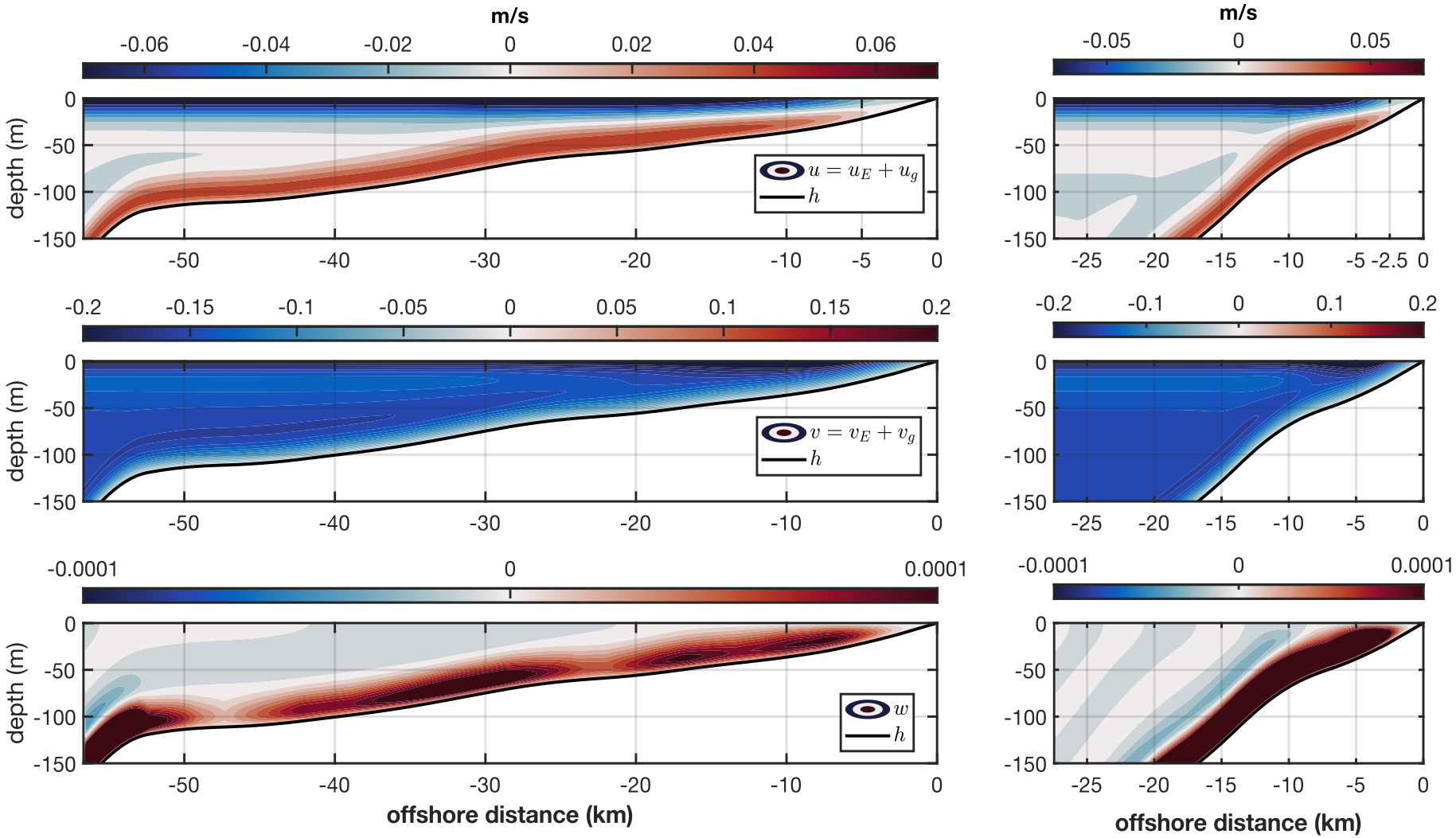

Figure 3.6: Velocities for $u_g = 0\,\mathrm{m\,s^{-1}}$: North and South locations are in the left and right column, respectively.

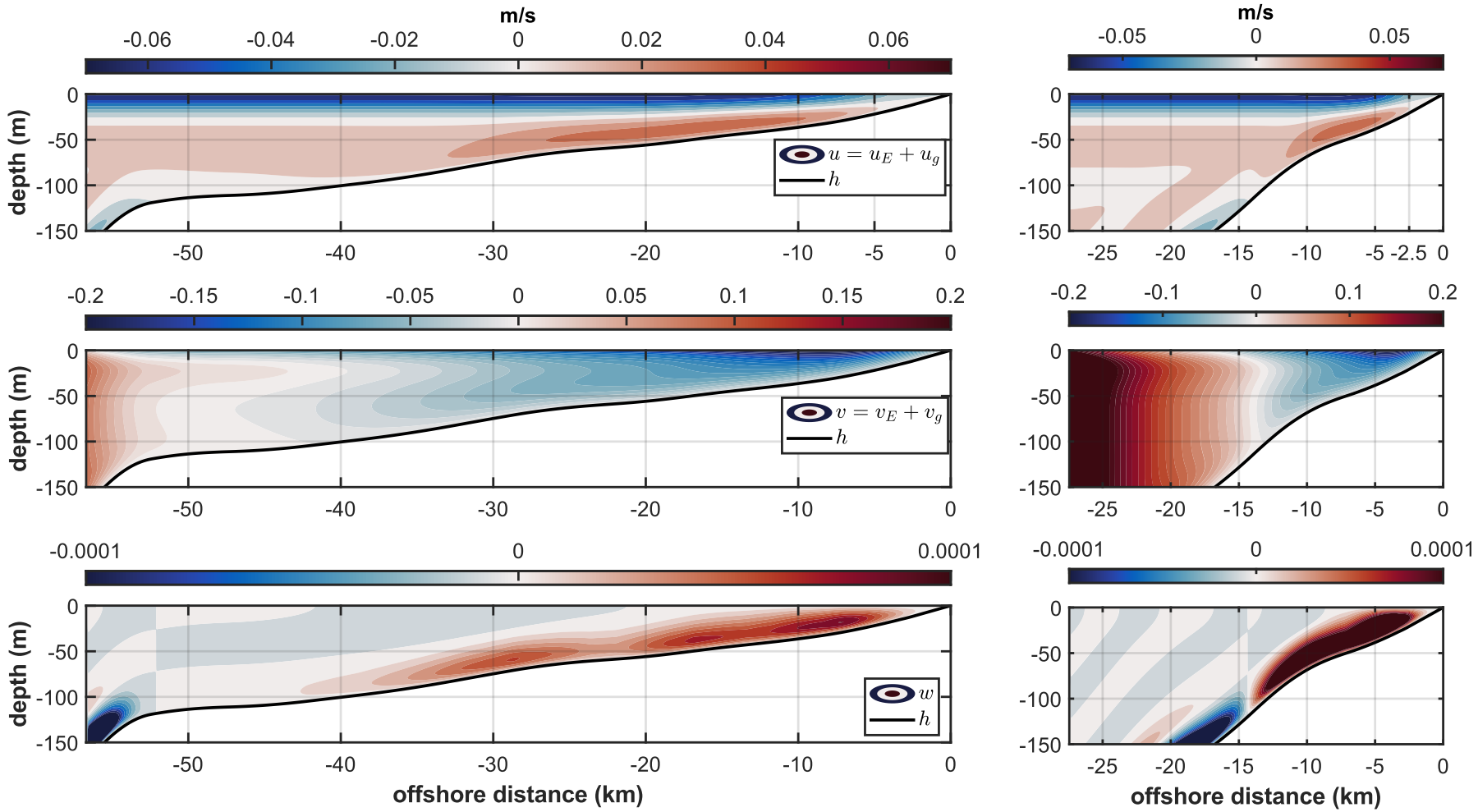

Figure 3.7: Velocities for $u_g = 0.01\,\mathrm{m\,s^{-1}}$: North and South locations are in the left and right column, respectively.

3.3.2 Upwelling indices

In this thesis, the study of the indices was performed for two fixed latitudes and a time span of eight years. More specifically, the indices were calculated for three months (June, July, and August) between 2000 and 2008. Marchesiello and Estrade (2010) performed a similar analysis, using an array of latitudes from various upwelling systems.

CUI and CUI–L_E

Almost all parameters used in the stream function computation are not available with detail in the nearshore region. Thus, interpolation of data had to be performed in order to obtain continuous data in the first kilometres (which are crucial to the analysis). A small summary of the datasets that were used is presented below.

u_g: Obtained from the Copernicus ECMWF dataset (`https://tinyurl.com/copernicusdataset`) which uses sea level anomaly to compute the geostrophic surface currents. The sea level anomaly is measured with respect to a twenty-year reference mean surface (1993–2012). The dataset has a $0.25° \times 0.25°$ resolution.

τ_x and τ_y: Obtained from the QuikSCAT dataset with $0.125°$ (`https://tinyurl.com/quikscatdataset`).

After extracting the `netcdf` files of the above stated variables for the two specified latitudes, interpolation followed. Regarding the geostrophic velocities dataset, fortunately, there was a point near the coast that saved the trouble of attributing an approximate value of the velocity at $x = 0$. Since the dataset only has daily values, a monthly mean had to be obtained. As it can be seen on **Figure 3.8**, for both North and South locations, upon plotting discrete values it was found that a simple second degree polynomial gave the best results. The average correlation coefficient was $r^2 = 0.9656$ for the South location and $r^2 = 0.9509$ for the North one. Is worth mentioning that u_g values for the South are almost always positive (onshore flow) and negative for the North locations (offshore flow). This means that large-scale offshore geostrophic flow favours upwelling in the North, whereas onshore geostrophic flow reduces upwelling in the South.

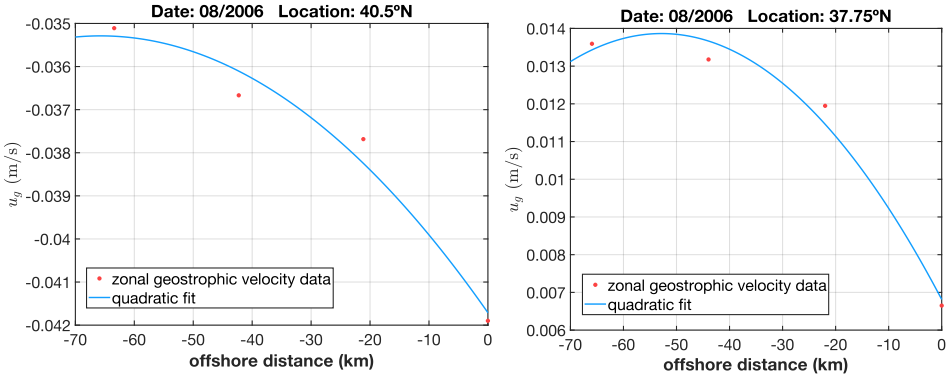

Figure 3.8: Example of the u_g interpolation for both locations

The article of Capet et al. (2004) shows that the profile of wind stress follows an exponential behaviour near the coast, giving rise to a strong wind drop-off, as shown in **Figure 3.9**. In view of this evidence, an attempt to fit a Gaussian curve to τ_y was made. However, the fit never seemed to work properly. Nevertheless, the results of the paper were used to have an estimate of τ_y at $x = 0$, which was set to be $(\tau_y)_{x=0} = -0.03\,\mathrm{Pa}$. The chosen fit was again a quadratic one, as illustrated in **Figure 3.10**. The average correlation coefficients for the South and North locations were $r^2 = 0.8846$ and $r^2 = 0.8017$, respectively.

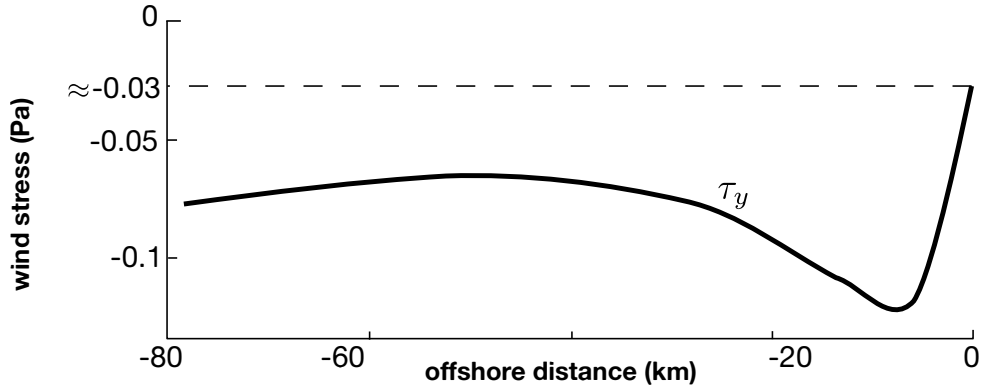

Figure 3.9: Meridional shear stress profile for a $3\,\mathrm{km}$ high-resolution model (COAMPS: Coupled Ocean/Atmosphere Mesoscale Prediction Systems) – adapted from Capet et al. (2004)

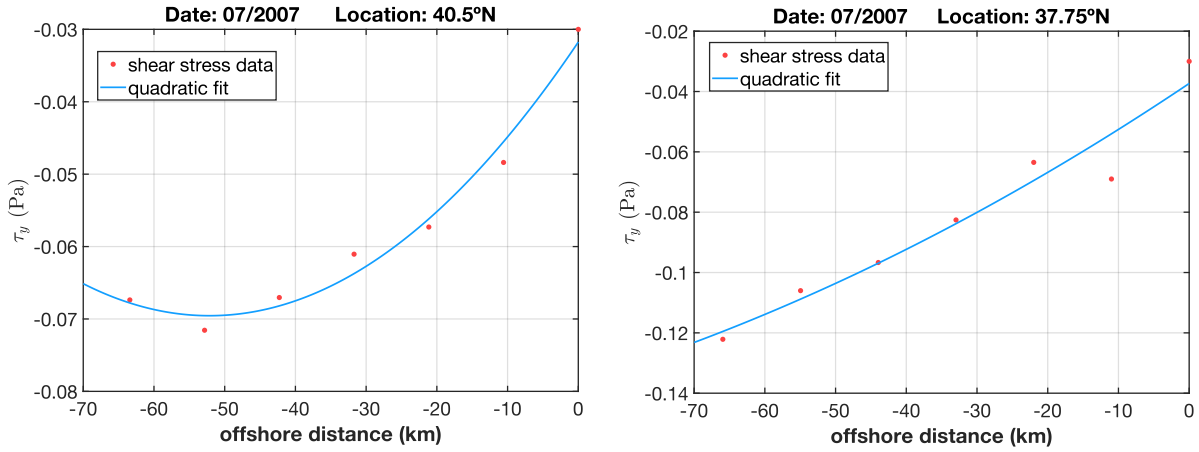

Figure 3.10: Example of the τ_y interpolation for both locations

When it comes to the cross-shore component of the wind shear stress, a cubic polynomial was fit to the data. The average correlation coefficients for the South and North locations were $r^2 = 0.8846$ and $r^2 = 0.8017$, respectively.

All variables that change with x, except h, have an analytical expression. The stream function and its x derivative (*i.e.* w) were calculated analytically using Wolfram Mathematica. Besides ρ_0, f, D, x, z, and h, the expression for w is a function of the fitting coefficients of all the interpolated variables and dh/dx, the slope. In fact, it is directly proportional to the slope. Since h does not have a simple analytical expression, numerical differentiation was used to calculate the slope.

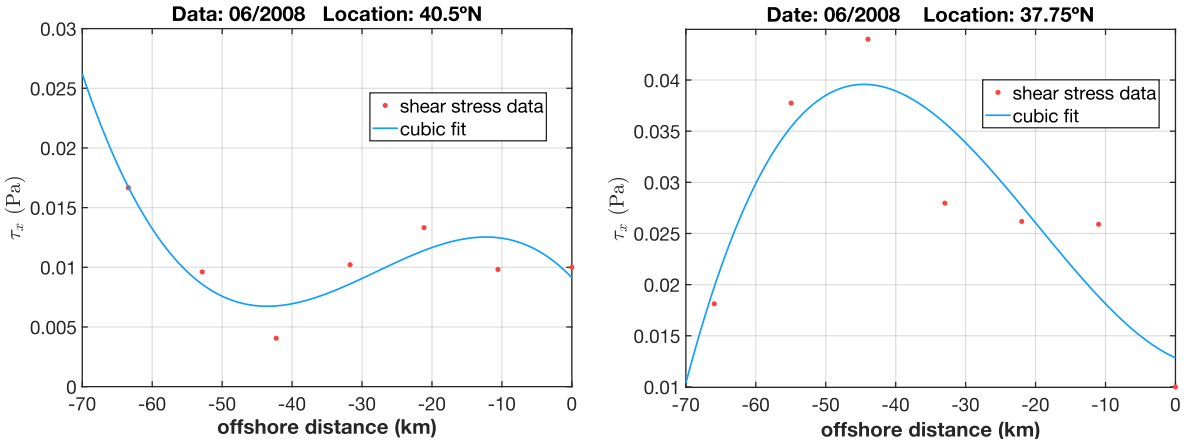

Figure 3.11: Example of the τ_x interpolation for both locations

This time in a MATLAB script, the vector that contains the bathymetry was differentiated according to:

$$\left(\frac{\partial h}{\partial x}\right)_{\text{cd}} \approx \frac{h_{i+1} - h_{i-1}}{x_{i+1} - x_{i-1}} \tag{3.13}$$

$$\left(\frac{\partial h}{\partial x}\right)_{\text{fd}} \approx \frac{h_{i+1} - h_i}{x_{i+1} - x_i} \tag{3.14}$$

$$\left(\frac{\partial h}{\partial x}\right)_{\text{bd}} \approx \frac{h_i - h_{i-1}}{x_i - x_{i-1}} \tag{3.15}$$

Equation 3.13 was used for all the middle nodes, **Equation 3.14** was used for the first node and **Equation 3.15** for the last one.

For each month, the script searches for the maximum w velocity over each of the bathymetries. Knowing its location $(x, z) = (x_0, z_0)$, the full array of w at depth z_0 is obtained. Integration is performed from $x = -L_U$ to $x = 0$ using a $1/3$ Simpson's rule and only retaining the points that are in the ocean, as it can be seen in **Figure 3.12**. The same is performed for CUI$-L_E$ with the appropriate modifications.

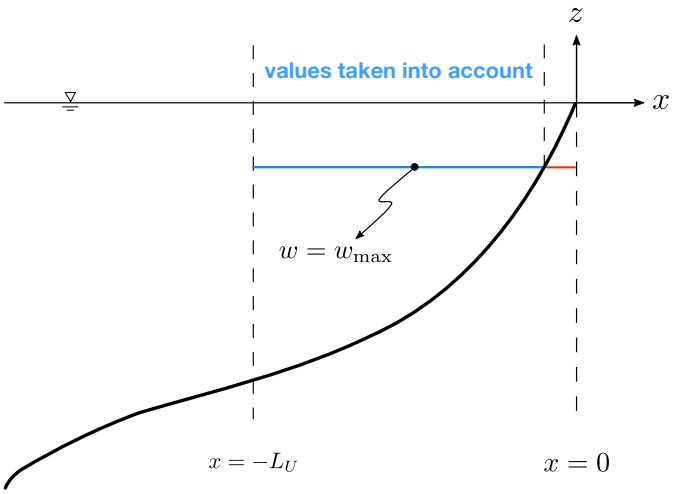

Figure 3.12: Scheme showing the w values taken into account in the CUI computation

Back in **Section 2.6.2**, CUI was defined with **Equation 2.13a**. Despite this correct theoretical definition, an equation that shows how CUI can be determined directly from the stream function is missing. The equation is simply:

$$\text{CUI} = \frac{1}{L_U} \int_{x_n=0}^{x_n=L_U} w(z_0)\, dx_n = \frac{1}{L_U} \int_{x_n=0}^{x_n=L_U} \left[\left(\frac{\partial \psi}{\partial x} \right)_{z=z_0} \right] dx_n \tag{3.16}$$

CUI is essentially a mean value of $w(z_0)$ over the region bounded by L_U. It should be mentioned that x-depending parameters such as $\tau_y(x)$ and $u_g(x)$ can still be included in the analytical model without losing the solution's validity.

SST–I

The temperatures required for this index have different time-scales, so it is important to detail each of the used datasets. The index is not only making use of a horizontal temperature difference at the surface, but also of a vertical temperature difference.

T: Obtained from the SST Pathfinder monthly composite (v5.2, L3C: `https://tinyurl.com/Tdataset`) which has a $0.0417°$ resolution.

T_0 and T_B: Obtained from the World Ocean Atlas 2018 (WOA18) dataset (`https://tinyurl.com/woa18dataset`). The decadal period from 1981–2010 with $1°$ resolution was selected.

As for the location where they must be evaluated, the paper of Marchesiello and Estrade (2010) is not completely clear. These were the definitions used for this thesis:

T: taken at $(x, z) = (x_0, 0)\ \mathrm{km}$

T_O: taken at $(x, z) = (-250, 0)\ \mathrm{km}$

T_B: taken at $(x, z) = (-250, -0.250)\ \mathrm{km}$

Figure 3.13 presents these locations merely as a scheme, no scaling was done. Again, x_0 is the x location of the point that has $w = w_{\max}$ between $x = -L_U$ and $x = 0$. T is the only temperature that changes position from month to month. For this reason, a script was written to check for the closest data point to x_0. The high-resolution of the SST Pathfinder dataset allowed for a near match most of the times.

In **Section 3.3.2**, it was written that the period of the analysis done in Marchesiello and Estrade (2010) was unknown. Despite this, it can be inferred that the study is indeed done for a climatological time window. Looking at p. 57, the authors write "*Finally, a non-dynamical index SST–I derived from satellite-based, AVHRR Pathfinder 9km SST climatology (...)* ". Since T_O and T_B are supposedly acquired from the WOA, this means that the remaining temperature T is taken from the AVHRR Pathfinder $9\,\mathrm{km}$ SST climatology dataset. It is thereby deduced that all three temperatures share a common climatological time-scale. Thus, for the sake of a meaningful comparison, all the other dynamical indices must have a climatological time-scale as well.

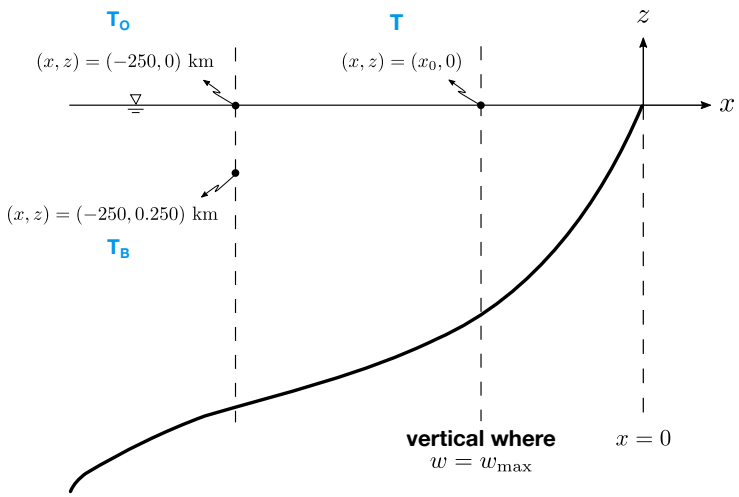

Figure 3.13: Scheme showing the location where the temperatures that make up SST−I are taken

Now, two issues must be highlighted: **(a)** the actual definition of SST−I and **(b)** the parameter $\triangle z/\gamma$.

(a) In this thesis, T is a SST chosen for the same vertical where $w_{\max}$ occurs, hence, it will naturally be a low temperature due to the ascent of cold waters. For ordinary upwelling circumstances, since T_O is a climatological mean temperature taken at a far offshore distance, it is foreseeable to obtain $T < T_O$. This implies that the index defined by Marchesiello and Estrade is positive in a downwelling situation and negative in an upwelling one. For this thesis, the absolute value of the index was taken in order to correct this.

(b) Marchesiello and Estrade took a fixed value of this parameter ($\triangle z/\gamma = 50\,\mathrm{m\,d^{-1}}$). For example, if $T \approx 16\,^{\circ}\mathrm{C}$, $T_O \approx 18\,^{\circ}\mathrm{C}$, and $T_B \approx 12\,^{\circ}\mathrm{C}$, the ratio $(T - T_O)/(T - T_B)$ is -0.5. Taking the absolute value of this result and multiplying it by $50\,\mathrm{m\,d^{-1}}$ gives SST−I $= 25\,\mathrm{m\,d^{-1}}$. This value is extremely high for the region in study.

In fact, Marchesiello and Estrade never obtained an SST−I as high as this one. There are various possible reasons for this:

(i) Acquiring T at x_0 is incorrect (there is no way to know if it is, since the authors did not specify their location) or perhaps the chosen dataset has inaccurate values nearshore.

(ii) For this thesis, T_O and T_B were obtained from the WOA18 objectively analysed climatologies (optimal interpolation). Another option were the statistical means. The chosen decadal period can be wrong, as the one used by Marchesiello and Estrade (2010) is unknown.

(iii) Marchesiello and Estrade smoothed all the indices with a $200\,\mathrm{km}$ low-pass cosine filter. This might have removed peaks from this particular index.

(iv) In the present study, T is a monthly average, while the other temperatures are climatological means. This can have an impact on the temporal consistency of the index, given that the authors used a climatological mean for all temperatures. The initial premise of this study's analysis was to show, for a span of 10 years, how the indices would change, therefore, it would not make sense to

change T into a climatological mean. The offshore temperature T_O can be easily obtained for a non-climatological monthly period, but the same cannot be said for T_B. A dataset that provides a monthly averaged subsurface temperature for every June, July, and August from 1999–2009 could not be found. This is why there was no other option and SST−I had to be evaluated using different time-scales for different temperatures.

In view of the above-mentioned reasons, the parameter $\triangle z/\gamma$ was changed in order to obtain significant values of SST−I. To lower this parameter, one must either decrease the subsurface depth (which then affects the location where T_B is taken), or increase the restoring time-scale γ. No other values of upwelling restoration time-scale could be found, so, despite the physical repercussions that might arise, γ was changed in order get plausible values of SST−I.

When showing the results, in order to avoid confusion, CUI−L_E will be omitted. For the South latitude CUI and CUI−L_E coincide. For the North latitude their evolution is identical, but CUI−L_E will always be higher in value due to the smaller region of integration.

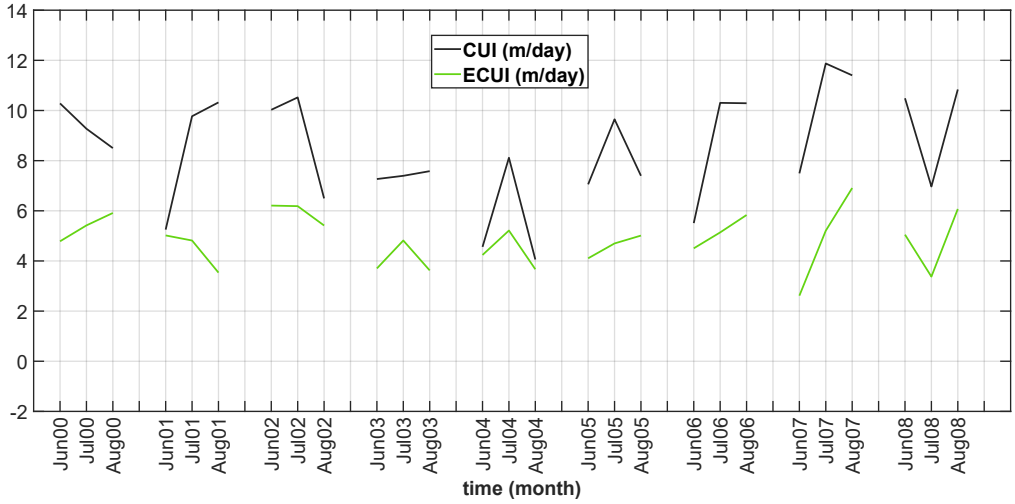

Figure 3.14: North location CUI and ECUI

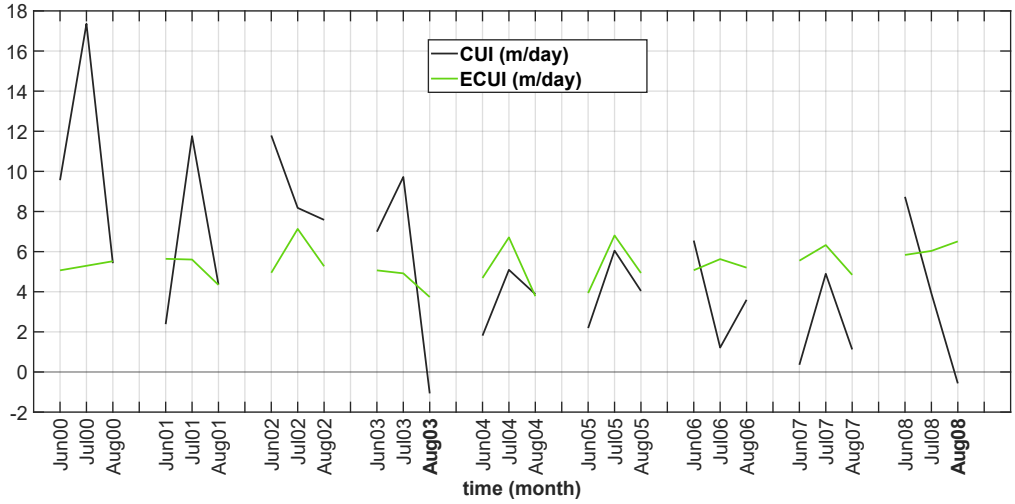

Figure 3.15: South location CUI and ECUI

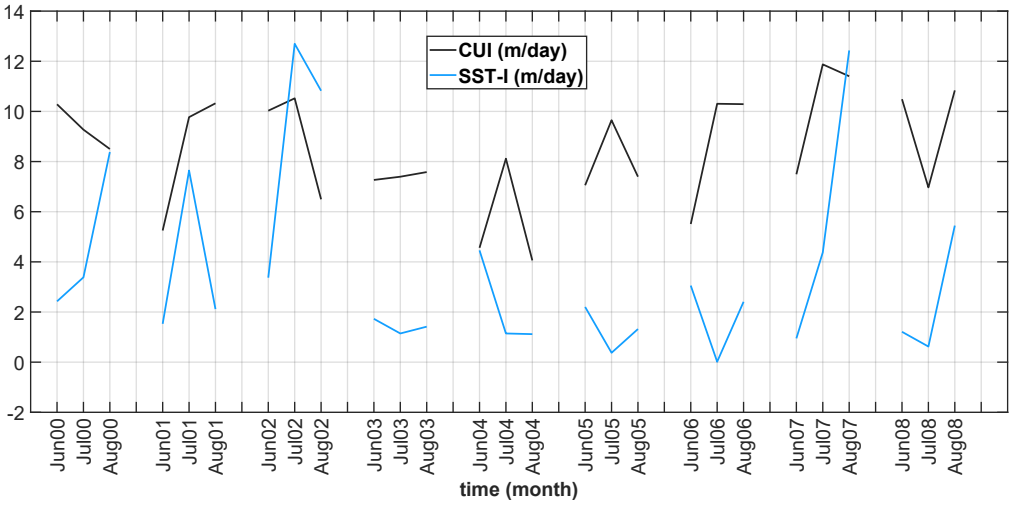

Figure 3.16: North location CUI and SST−I

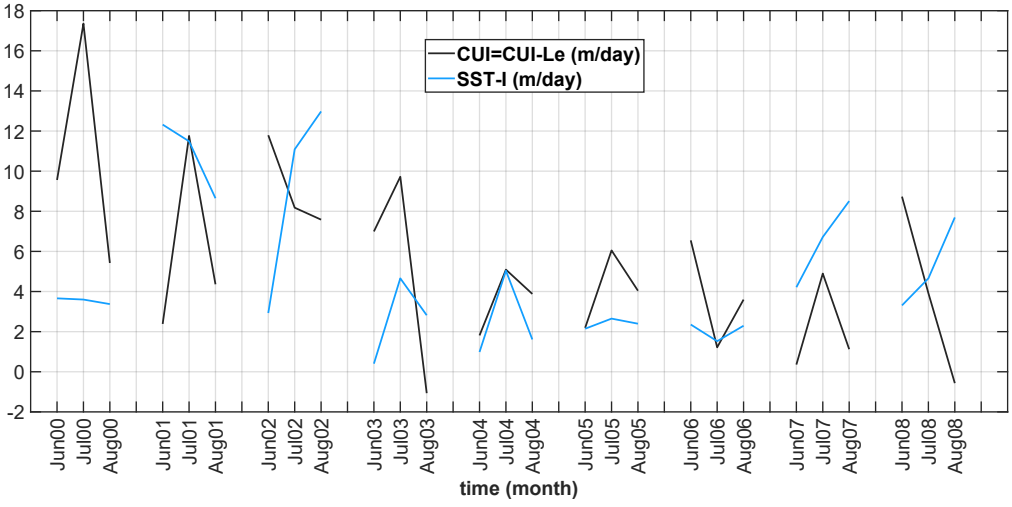

Figure 3.17: South location CUI and SST−I

Chapter 4

Discussion

4.1 Upwelling separation and kinematic barrier

The differences in the width of the kinematic barrier are not extremely large between the two study locations. In real life, for the broad shelf, the changes in D, which is a function of the flow, might end up dictating a lot of the upwelling separation. Assuming a constant, and in fact equal K_H, for both locations is, undoubtedly, a great simplification.

4.2 Indices

At this point it is important to say that the selection of datasets for this study was, above all, conditioned by the wind stress. After all, this is the main driving force of upwelling in the inner shelf. Between the old QuikSCAT and the more recent ASCAT dataset, the former was chosen due to its higher resolution near shore. Hence, all the other datasets were restricted to the time period of available QuikSCAT data (1999–2009).

Upon calculating SST−I, anomalous peaks in its intensity were found for two months. Since a higher-resolution dataset was also available at the time they took place, a comparison was made to find what was happening. Results from the Multi-scale Ultra-high Resolution (MUR) SST Monthly Analysis (2002-present, fv04.1, Global, $0.01°$) are presented in **Figure 4.1**, which shows the evolution of SST with longitude for August of 2007, one of the anomalous months. Upon comparison with the data from the SST Pathfinder, shown in **Figure 4.2**, at least one clear outlier can be seen. The closest temperature to x_0, which coincides with the right-most temperature recorded by the dataset, is exceptionally low, $T \approx 14\,^{\circ}\mathrm{C}$. As a consequence, instead of using the SST Pathfinder dataset, from 2002 onwards, values of T are obtained with the MUR dataset.

Before comparing the indices for both locations, the importance of the bathymetry and geostrophy roles must be shown.

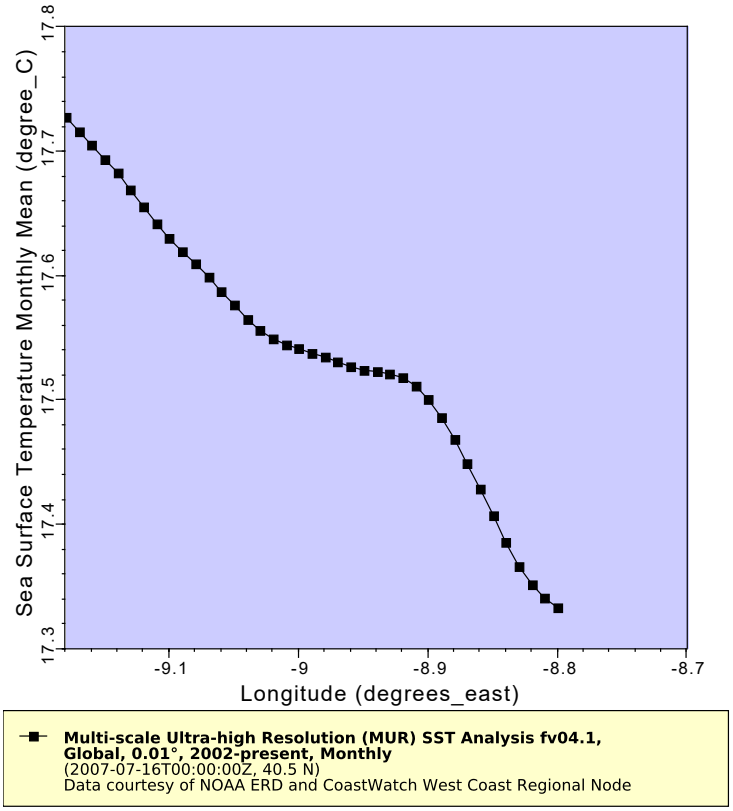

Figure 4.1: SST data from `https://tinyurl.com/MURdataset` for $40.50\,^{\circ}\mathrm{N}$

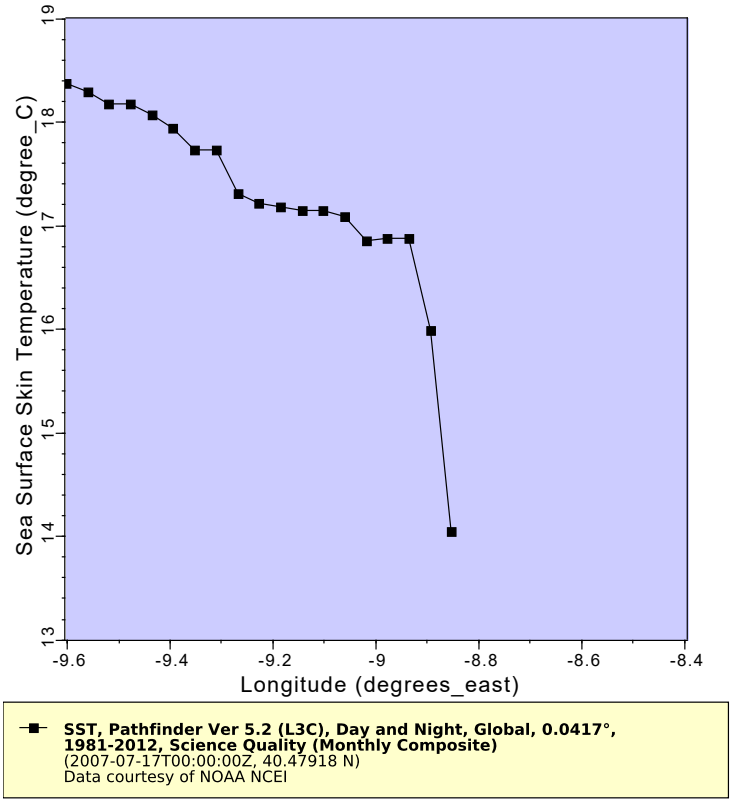

Figure 4.2: SST data from `https://tinyurl.com/Tdataset` for $40.50\,^{\circ}\mathrm{N}$

Regarding bathymetry, CUI was calculated for the North location using the locations' inputs (u_g, τ_y, τ_x, $h(x)$, f, and D). The next step was to freeze all the inputs except for f and $h(x)$, which are taken to be of the South location. As it can be seen in **Figure 4.3**, recalculating the index shows how the steeper shelf of the South location increases CUI.

As for the geostrophy, two simulations of CUI for the North latitude were done: one with the influence of geostrophic flow (which is almost always offshore) and the other with a non-existing geostrophic flow. Looking at **Figure 4.4**, it is clear that the offshore geostrophic flow in the North location favours upwelling.

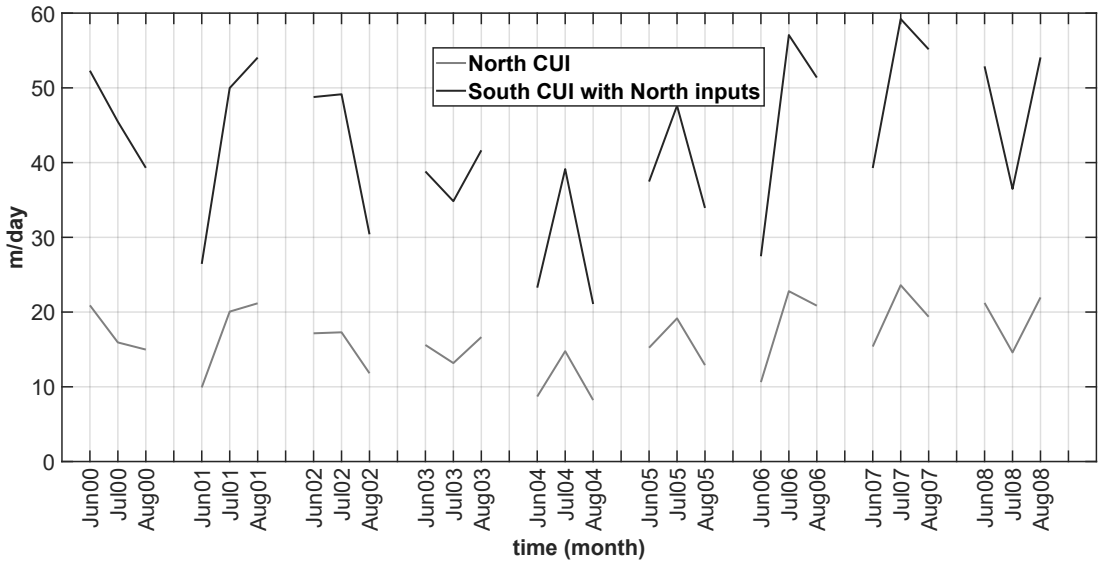

Figure 4.3: Comparison between CUI evaluated with different bathymetries — a steeper shelf favours upwelling

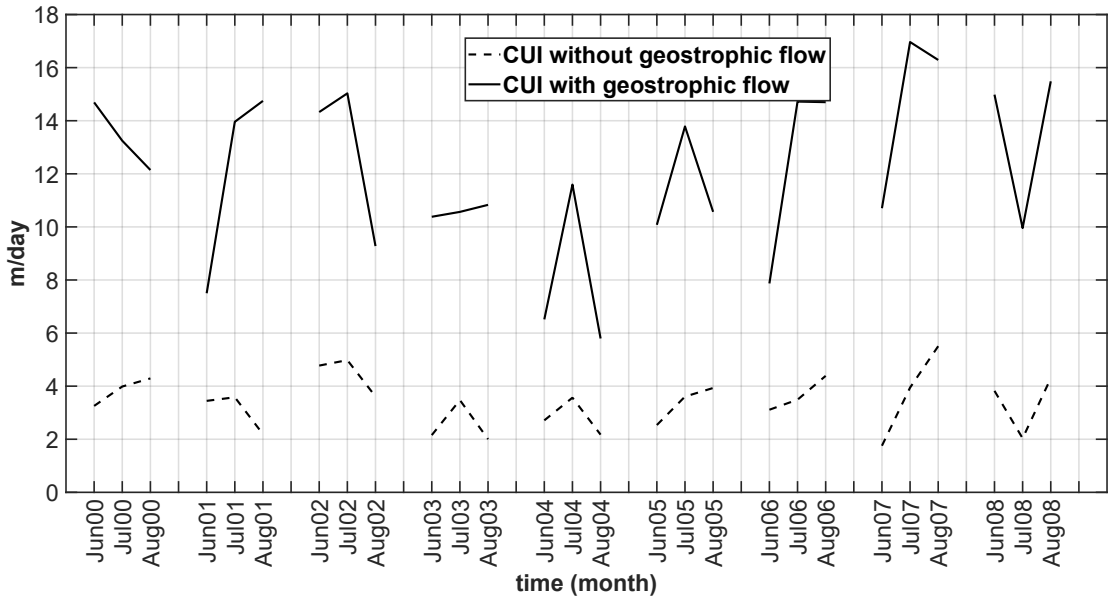

Figure 4.4: Comparison between CUI evaluated with and without geostrophic flow — offshore geostrophic flow favours upwelling

4.2.1 South location

Figure 3.15 reveals two unexpected downwelling situations in August of both 2003 and 2008. Regardless of their low index value, they are quite an unusual sight. The first step was to plot the vertical velocity w for the referred periods plus an additional month, June of 2003. The latter serves as a means to ascertain results, given its standard upwelling index value.

Figures 4.5 and **4.6** reveal a small upwelling region present in the first few kilometres, but the majority of vertical velocities until the $x = -5\,\mathrm{km}$ mark are mostly negative. It should be remembered that CUI is a mean of $w(z_0)$ over the region that extends from the coast to $x = -L_U$ (excluding land points). Thus, if inside the aforementioned limits, w is mainly negative, the index will be negative as well. As for **Figure 4.7**, a positive vertical velocity follows the shelf slope, representing the usual situation. These contours can be compared to **Figure 3.6**, which shows the same equation plotted for constant u_g and τ_y. To figure out the reason (or reasons) for such pronounced negative vertical velocities in **Figures 4.5** and **4.6**, a quick inspection to $\tau_y(x)$ and $u_g(x)$ plots was conducted.

Figures 4.8, **4.9**, and **4.10** show how the geostrophic onshore flow has a remarkable impact in the flow structure. Taking a look at the bottom right corner of **Figure 3.7**, which was plotted for approximately half of the value of u_g, it is almost as if the the negative (blue) contours spread over the shelf and "push" the upwelling cell against the shore.

The values of τ_y for August 2008 are higher than those of 2003, which explains why the magnitude of the vertical velocities is higher in the former year.

Looking at **Figure 3.15**, from August 2003 onwards the black line (CUI) is always under the green one (ECUI) except for some months. This means that from that date onwards, the onshore geostrophic flow is lowering the vertical velocities that make up CUI. As for **Figure 3.17**, the indices' tendencies do not agree with each other for the most part.

The article of Marchesiello and Estrade (2010) presented a new index, CUI, as a better alternative to the traditional Bakun index (ECUI). Unfortunately, with this thesis' approach one cannot prove that. In the years like 2000, where ECUI and CUI have opposite tendencies, one would need a reliable index to decide which one is closer to representing the reality. It is true that SST−I (blue line) could be a way to untie between the black line and the green line, but since the index itself was so hard to evaluate, its role as the closest index to reality is highly questionable.

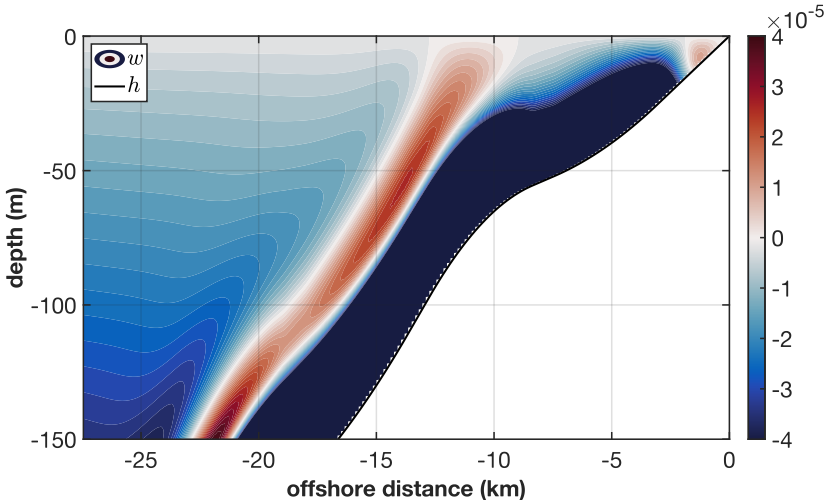

Figure 4.5: Vertical velocity w plotted for $08/2003$ at $37.75\,°\mathrm{N}$

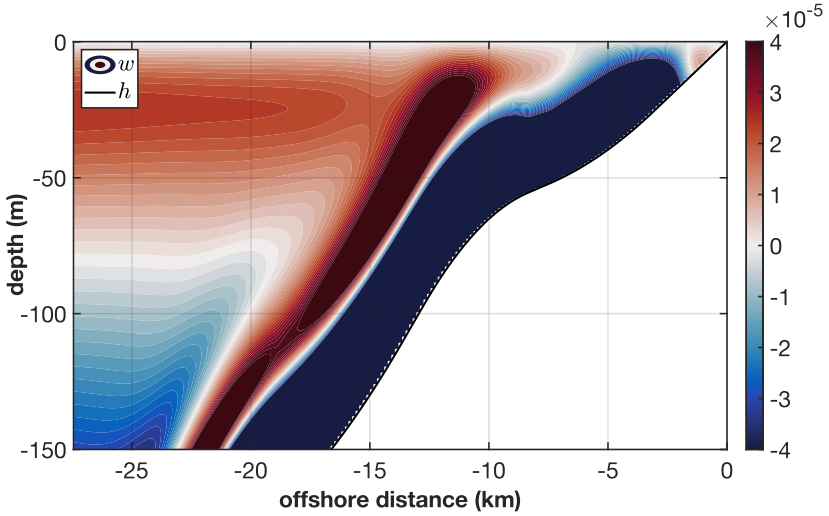

Figure 4.6: Vertical velocity w plotted for $08/2008$ at $37.75\,°\mathrm{N}$

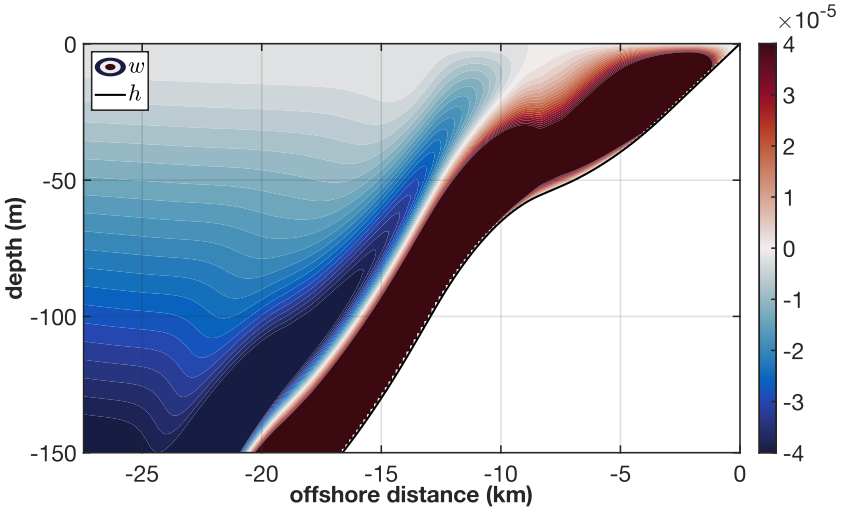

Figure 4.7: Vertical velocity w plotted for $06/2003$ at $37.75\,°\mathrm{N}$

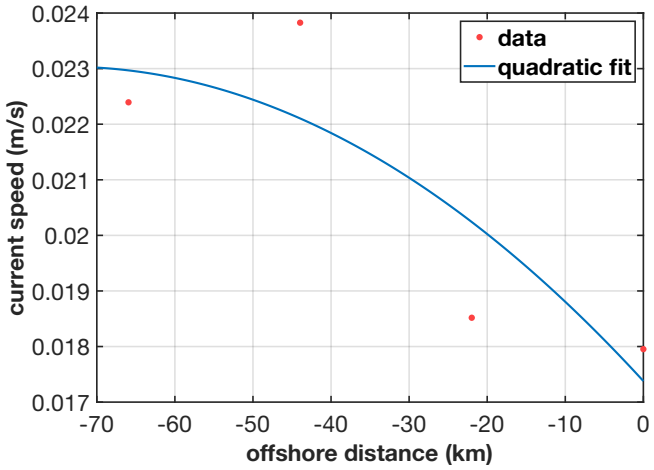

Figure 4.8: Zonal geostrophic flow u_g plotted for $08/2003$ at $37.75\,^{\circ}\mathrm{N}$

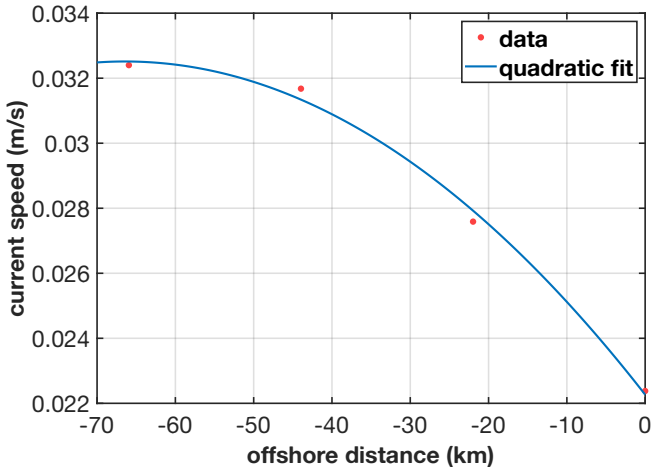

Figure 4.9: Zonal geostrophic flow u_g plotted for $08/2008$ at $37.75\,^{\circ}\mathrm{N}$

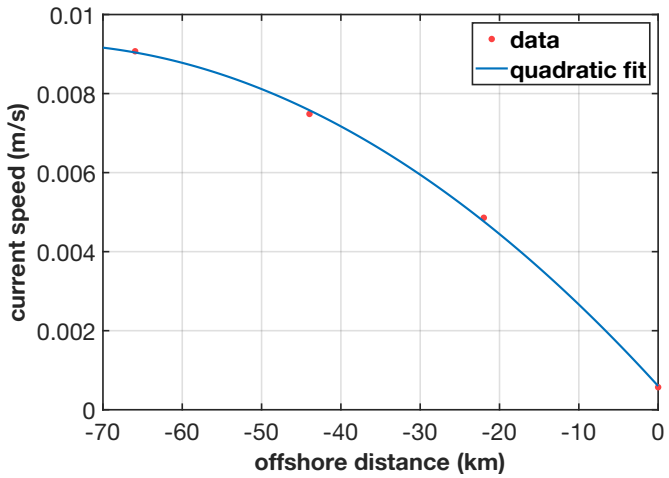

Figure 4.10: Zonal geostrophic flow u_g plotted for $06/2003$ at $37.75\,^{\circ}\mathrm{N}$

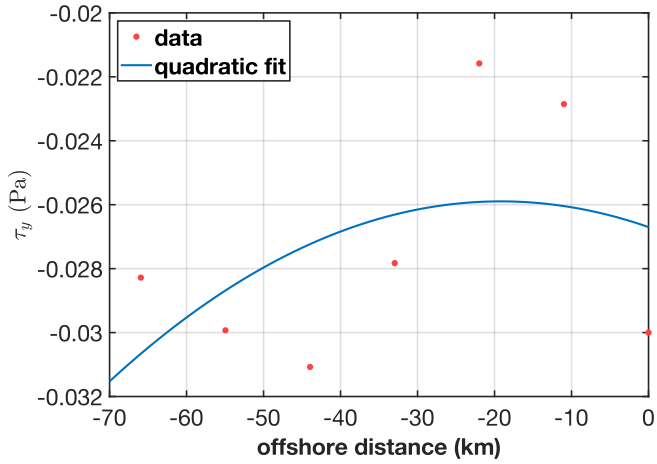

Figure 4.11: Meridional wind stress τ_y plotted for $08/2003$ at $37.75\,°\mathrm{N}$

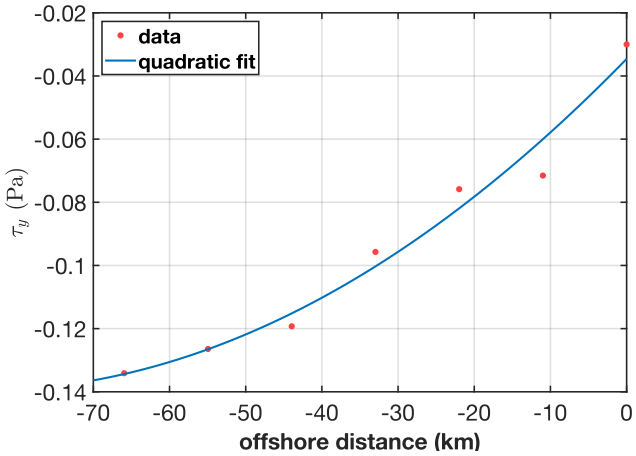

Figure 4.12: Meridional wind stress τ_y plotted for $08/2008$ at $37.75\,°\mathrm{N}$

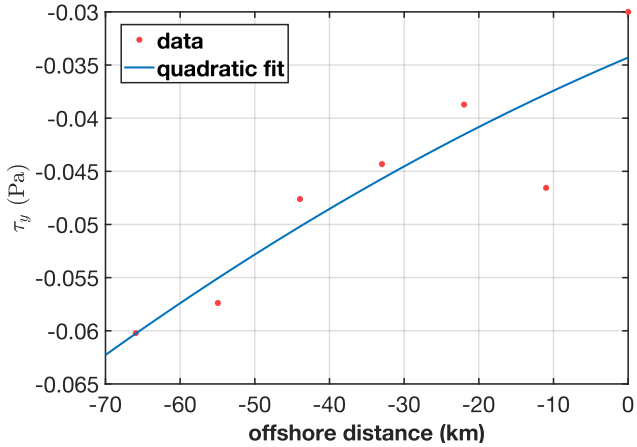

Figure 4.13: Meridional wind stress τ_y plotted for $06/2003$ at $37.75\,°\mathrm{N}$

4.2.2 North location

Looking at **Figure 3.14**, the black line (CUI) is always above the green one (ECUI). This means that thee offshore geostrophic flow is increasing the vertical velocities that make up CUI. In other words, geostrophy is favouring upwelling.

Regarding **Figure 3.16**, for the period of 2004–2006 the correlation is quite bad: the tendencies are opposite of one another. In 2008, there is an agreement between the indices. During 2003, both indices do not change much.

4.3 Possible error sources

In this study, the major source of errors is likely related to the near shore interpolation. For instance, attributing a value to the wind stress at $x = 0$ is obviously a bold assumption, although a much-needed one. Marchesiello and Estrade (2010), in all likelihood, used a higher quality interpolation method. Despite this, cubic splines, or some other potentially more powerful methods seemed unsuitable. Mostly because in order to maintain an analytical representation of the stream function (using interpolation coefficients), the fit's analytical expression has to be easily obtained. Choosing a quadratic polynomial has advantages when computing the stream function, but features like the wind drop-off near the coast are lost.

Another important point stated by Marchesiello and Estrade is the geostrophic flow calculation. In this thesis, the u_g surface current was obtained directly from a dataset, whereas Marchesiello and Estrade did their calculation using density profiles and sea-surface elevation data. The authors reckon that this aspect remains a source of uncertainty in their computation.

The analysis done in Marchesiello and Estrade (2010) freezes the time variable in order to study a span of latitudes, whilst in this thesis the space dimension is restricted to two latitudes and the time variable is free. Nevertheless, it is interesting to look at the results obtained by the authors for the CIUE. The results are on page 58, top right corner. The values are much lower than those obtained in this study, most probably due to the large climatological time window. Naturally, their study ends up taking into consideration many years and all the other months besides June, July and August, where the upwelling phenomenon is uncommon in the Portuguese coast. The filter applied by the authors is also different than the one used in this work.

Bathymetry is also a sensitive topic. Without smoothing, the stream function contours will become quite jagged. Of course, smoothing the bathymetry will also change dh/dx, which is directly proportional to vertical velocities that make up the CUI and CUI–L_E.

The same can be said for the integration method. It is relevant to point out that, before the $1/3$ Simpson rule, a simpler trapezoidal rule was tested. The results were different enough to show a slight deviation of the CUI and CUI–L_E lines in the South location, where they theoretically coincide.

4.4 Comparison of indices between the North and the South

Figure 4.14 shows how the Bakun (ECUI) indices for both locations tend to agree on their evolution. The sea surface temperature based index (SST−I), on the contrary, does not agree so nicely from North to South, but it is interesting to notice that 2002 and 2007 are both years where the index has a peak in intensity.

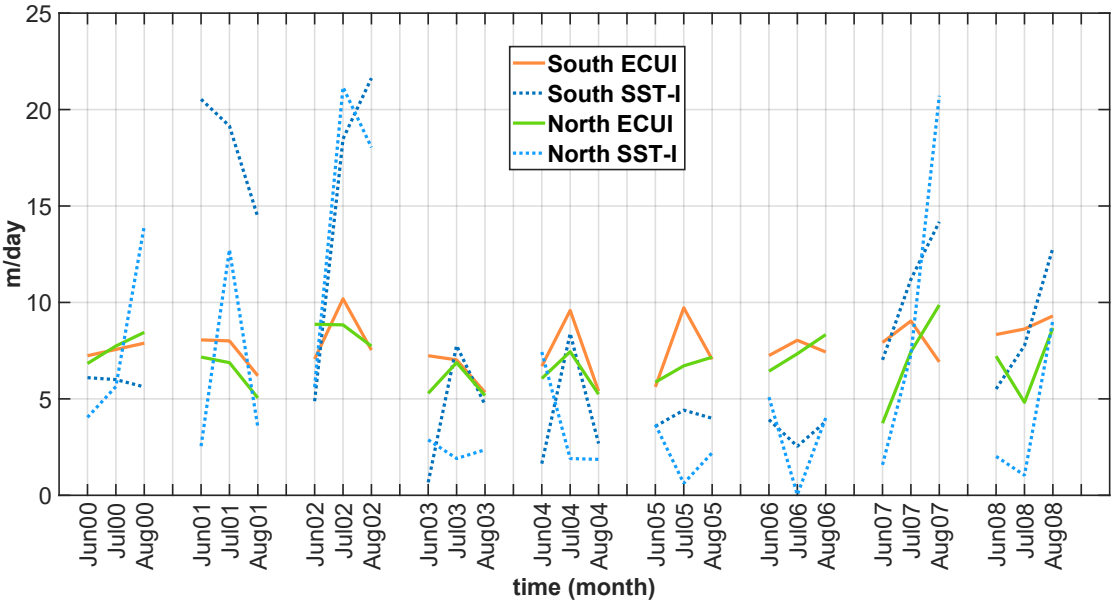

Figure 4.14: Index comparison between the two studied locations

Chapter 5

Conclusions

5.1 Achievements

Unveiling the potentially dictating role of geostrophic flow on upwelling during the summertime, especially in the South study location, was the major achievement of this thesis.

The studied North location has a predominantly offshore geostrophic current which favours upwelling, while the exact opposite happens on the South location. As a consequence, ECUI and SST−I curves are similar in both coasts, whilst CUI and CUI−L_E vary greatly.

5.2 Future Work

Good results will always rely on good data in the nearshore region, specifically shear stress. High-quality datasets together with a more robust interpolation could be a way to improve results.

Checking the influence of stratification and friction is a task yet to be tackled. Using a numerical model, like MOHID for instance, can be an important step to verify the influence of the stated mechanisms in the analytical model, just as done in Marchesiello and Estrade (2010).

Studying other locations is a possibility, but the Portuguese coast can be tricky. The analytical model, which requires a steady-state and a two-dimensional approach, will not produce good results close to great bathymetric accidents, like the Nazaré or Aveiro canyons. Nonetheless, should other locations be object of study, the dynamical indices will, presumably, present a higher correlation where the geostrophic onshore flow effect is not taken into account.

The hindering of upwelling situations observed in the south-western Portuguese coast could potentially be verified for a smaller time scale (daily, instead of monthly) using SST imagery or even checking for blooms in phytoplankton. A more in-depth study of how geostrophic flow behaves in the offshore regions of the IP could also be of interest.

All things considered, the dynamical upwelling indices depend mostly upon three parameters: bathymetry, zonal geostrophic flow, and meridional shear stress.

Bathymetry, in the case of this study, does not affect the structure of upwelling significantly. Despite this, if all the other parameters are constant, it should be said that in the South coast, the vertical velocities are higher due to the steeper slope.

As for the wind stress, the monthly values are always negative (for June, July, and August) in the studied locations. The values obtained with interpolation are always higher in the South coast.

On a final note, the restraining effects of onshore geostrophic flow in the south-western Portuguese coast remains, by far, the most intriguing result to be confirmed with potential subsequent studies.

Bibliography

Bakun, A. (1990). Coastal Ocean Upwelling. *Science*, 247(4939):198–201.

Bakun, A., Dickson, R. R., Maelkki, P., Radach, G., Saetre, R., and Sissenwine, M. P. (1992). Global greenhouse effects, multi-decadal wind trends, and potential impacts on coastal pelagic fish populations. pages 316–325.

Batteen, M. L., Lopes, C. N., and Nelson, C. S. (1992). A numerical study of wind stress curl effects on eddies and filaments off the northwest coast of the Iberian Peninsula. 3:249–266.

Capet, X. J., Marchesiello, P., and McWilliams, J. C. (2004). Upwelling response to coastal wind profiles. *Geophysical Research Letters*, 31(13):1–4.

DeCastro, M., Gómez-Gesteira, M., Lorenzo, M. N., Alvarez, I., and Crespo, A. J. (2008). Influence of atmospheric modes on coastal upwelling along the western coast of the Iberian Peninsula, 1985 to 2005. *Climate Research*, 36(2):169–179.

Ekman, V. W. (1905). On the Influence of the Earth's Rotation on Ocean-Currents.

Estrade, P., Marchesiello, P., De Verdière, A. C., and Roy, C. (2008). Cross-shelf structure of coastal upwelling: A two-dimensional extension of Ekman's theory and a mechanism for inner shelf upwelling shut down. *Journal of Marine Research*, 66(5):589–616.

EUMOFA (2019). The EU Fish Market Highlights - The EU Market Supply, Consumption, Import and Export, EU Landings and Aquaculture Production. Technical report.

Fiuza, A. F. G., Macedo, M. E., and Guerreiro, M. R. (1982). Climatological space and time variation of the Portuguese coastal upwelling Upwelling Portugal Coastal winds Sea surface temperature Sardine Upwelling Portugal Vents côtiers Température de surface de la mer Sardine ABSTRACT RÉSUMÉ. *Oceanologia Acta*, 5(1):31–40.

Gaertner, M. A., Fernandez, C., and Castro, M. (1993). A two-dimensional simulation of the Iberian summer thermal low. *Monthly Weather Review*, 121(10):2740–2756.

Haynes, R., Barton, E. D., and Pilling, I. (1993). Development, persistence, and variability of upwelling filaments off the Atlantic coast of the Iberian Peninsula. *Journal of Geophysical Research*, 98(C12).

Jin, X., Dong, C., Kurian, J., McWilliams, J. C., Chelton, D. B., and Li, Z. (2009). SST-wind interaction in coastal upwelling: Oceanic simulation with empirical coupling. *Journal of Physical Oceanography*, 39(11):2957–2970.

Marchesiello, P. and Estrade, P. (2010). Upwelling limitation by onshore geo strophic flow. *Journal of Marine Research*, 68(1):37–62.

Mason, E., Coombs, S., and Oliveira, P. (2006). An overview of the literature concerning the oceanography of the eastern North Atlantic region. Technical report.

Miranda, P. M., Alves, J. M., and Serra, N. (2013). Climate change and upwelling: Response of Iberian upwelling to atmospheric forcing in a regional climate scenario. *Climate Dynamics*, 40(11-12):2813–2824.

Monteiro, I. T., Santos, A. J., Belo-Pereira, M., and Oliveira, P. B. (2016). Adjustment of the summertime marine atmospheric boundary layer to the western Iberia coastal morphology. *Journal of Geophysical Research: Atmospheres*, 120(8):3875–3893.

Peliz, Á., Rosa, T. L., Santos, A. M. P., and Pissarra, J. L. (2002). Fronts, jets, and counter-flows in the Western Iberian upwelling system. *Journal of Marine Systems*, 35(1-2):61–77.

Pingree, R. D. and Le Cann, B. (1992). Three anticyclonic slope water oceanic eDDIES (SWODDIES) in the Southern Bay of Biscay in 1990. *Deep Sea Research Part A, Oceanographic Research Papers*, 39(7-8):1147–1175.

Relvas, P., Barton, E. D., Dubert, J., Oliveira, P. B., Peliz, Á., da Silva, J. C., and Santos, A. M. P. (2007). Physical oceanography of the western Iberia ecosystem: Latest views and challenges. *Progress in Oceanography*, 74(2-3):149–173.

Richardson, P. L., Bower, A. S., and Zenk, W. (2000). A census of Meddies tracked by floats. *Progress in Oceanography*, 45(2):209–250.

Shanks, A. L., Largier, J., Brink, L., Brubaker, J., and Hooff, R. (2000). Demonstration of the onshore transport of larval invertebrates by the shoreward movement of an upwelling front. *Limnology and Oceanography*, 45(1):230–236.

Simpson, J. H., Crisp, D. J., and Hearn, C. (1981). The shelf-sea fronts: implications of their existence and behaviour. *Philosophical Transactions of the Royal Society of London. Series A, Mathematical and Physical Sciences*, 302(1472):531–546.

Stewart, R. H. (2012). *Introduction to Physical Oceanography*.

Teles-Machado, A., Peliz, Á., McWilliams, J. C., Couvelard, X., and Ambar, I. (2016a). Circulation on the Northwestern Iberian Margin: Vertical structure and seasonality of the alongshore flows. *Progress in Oceanography*, 140:134–153.

Teles-Machado, A., Peliz, Á., McWilliams, J. C., Dubert, J., and Cann, B. L. (2016b). Circulation on the Northwestern Iberian Margin: Swoddies. *Progress in Oceanography*, 140(December):116–133.

The Open University, Brown, J., Colling, A., Park, D., Phillips, J., Rothery, D., and Wright, J. (1989). *Ocean Circulation*. Butterworth Heinemann, in association with The Open University, 1st edition.

Trujillo, A. P. and Thurman, H. V. (2017). *Essential Of Oceanography*.

Welander, P. (1957). Wind Action on a Shallow Sea: Some Generalizations of Ekman's Theory. *Tellus*, 9(1):45–52.

Winant, C. D., Dorman, C. E., Friehe, C. A., and Beardsley, R. C. (1988). The marine layer off northern California: an example of supercritical channel flow. *Journal of the Atmospheric Sciences*, 45(23):3588–3605.

Appendix A

Derivation of the analytical model main equations

A.1 Horizontal flow field

To understand how the solution is derived, it is useful to start with the full equations of momentum:

$$\frac{\partial u}{\partial t} + u\frac{\partial u}{\partial x} + v\frac{\partial u}{\partial y} + w\frac{\partial u}{\partial z} = -\frac{1}{\rho_0}\frac{\partial p}{\partial x} + fv + \frac{1}{\rho_0}\left(\frac{\partial \tau_{xx}}{\partial x} + \frac{\partial \tau_{yx}}{\partial y} + \frac{\partial \tau_{zx}}{\partial z}\right) \tag{A.1a}$$

$$\frac{\partial v}{\partial t} + u\frac{\partial v}{\partial x} + v\frac{\partial v}{\partial y} + w\frac{\partial v}{\partial z} = -\frac{1}{\rho_0}\frac{\partial p}{\partial y} - fu + \frac{1}{\rho_0}\left(\frac{\partial \tau_{xy}}{\partial x} + \frac{\partial \tau_{yy}}{\partial y} + \frac{\partial \tau_{zy}}{\partial z}\right) \tag{A.1b}$$

The simplifying assumptions for **Equations A.1a** and **A.1b** are not the same as Ekman's, as the first derivation in his paper only deals with the drift current (balance between Coriolis and friction forces). Because the stream function that will be derived accounts for the geostrophic flow as well, pressure must remain in the force balance. The wind shear stress is not involved in the balance because it only acts on the boundary, whether Coriolis forces, friction and pressure act upon all particles. Therefore, wind shear stress enters only as a boundary condition.

Assumptions:

(i) steady state ($\partial/\partial t = 0$)

(ii) $\mathrm{Ro} \ll 1$ (negligible advection)

(iii) $H/L \ll 1$ (typical ocean basin)

(iv) barotropic ocean

(v) $K_V = \mathrm{const}$

(vi) $2D$ ocean ($\partial/\partial y = 0$)

(vii) $(K_H)_x \gg K_V$ or $(\mathrm{Ek}_H)_x \ll \mathrm{Ek}_V$

Under the second assumption, $\tau_{xx}, \tau_{xy}, \tau_{yy}, \tau_{yx} \ll \tau_{zx}, \tau_{zy}$. The argument $H/L \ll 1$ can be used again together with the continuity equation for incompressible flow to further simplify the relevant shear stresses:

$$\mathcal{O}\left(\frac{\partial u}{\partial x}+\frac{\partial v}{\partial y}+\frac{\partial w}{\partial z}\right)=\frac{U}{L}+\frac{U}{L}+\frac{W}{H}\sim 0 \Leftrightarrow W\sim\frac{UH}{L} \tag{A.2a}$$

$$\tau_{zx}=\mu\left(\frac{\partial u}{\partial z}+\frac{\partial w}{\partial x}\right)\ \therefore\ \mathcal{O}\left(\tau_{zx}\right)=\frac{U}{H}+\frac{W}{L}\sim\frac{U}{H}+\frac{\frac{UH}{L}}{L}\sim\frac{U}{H}+\frac{U}{L}\frac{H}{L}\sim\frac{U}{H} \tag{A.2b}$$

$$\tau_{zx}=\mu\left(\frac{\partial u}{\partial z}+\frac{\partial w}{\partial x}\right)\approx\mu\frac{\partial u}{\partial z} \tag{A.2c}$$

$$\tau_{zy}=\mu\left(\frac{\partial v}{\partial z}+\frac{\partial w}{\partial y}\right)\approx\mu\frac{\partial v}{\partial z} \tag{A.2d}$$

Rewriting **Equations A.1a** and **A.1b**, a molecular viscosity $\nu = \mu/\rho_0$ should appear, but since the turbulent exchange of momentum dominates over it, the eddy viscosity coefficient K comes up instead:

$$-\frac{1}{\rho_0}\frac{\partial p}{\partial x}+fv+K_V\frac{\partial^2 u}{\partial z^2}=0 \tag{A.3a}$$

$$-\frac{1}{\rho_0}\frac{\partial p}{\partial y}-fu+K_V\frac{\partial^2 v}{\partial z^2}=0 \tag{A.3b}$$

Equations A.3 can be merged into a single differential equation using complex notation.

$$\begin{cases}\tilde{u}=u+iv\\ \frac{\partial\tilde{p}}{\partial n}=\frac{\partial p}{\partial x}+i\frac{\partial p}{\partial y}\\ \tilde{\tau}^s=\tau_x^s+i\tau_y^s\end{cases} \tag{A.4}$$

Multiplying **Equation A.3b** by the imaginary unit i and adding it to **Equation A.3a** gives:

$$\begin{cases}-\frac{1}{\rho_0}\frac{\partial p}{\partial x}+fv+K_V\frac{\partial^2 u}{\partial z^2}=0\\ -\frac{1}{\rho_0}i\frac{\partial p}{\partial y}+fiu+K_V\frac{\partial^2 (iv)}{\partial z^2}=0\end{cases}\quad\Leftrightarrow -\frac{1}{\rho_0}\frac{\partial p}{\partial x}-\frac{1}{\rho_0}i\frac{\partial p}{\partial y}+fv-fiu+K_V\frac{\partial^2 u}{\partial z^2}+K_V\frac{\partial^2 (iv)}{\partial z^2}=0$$

$$\Leftrightarrow -\frac{1}{\rho_0}\left(\frac{\partial p}{\partial x}+i\frac{\partial p}{\partial y}\right)+f(v-iu)+K_V\frac{\partial^2 (u+iv)}{\partial z^2}=0 \tag{A.5}$$

$$\Leftrightarrow -\frac{1}{\rho_0}\frac{\partial\tilde{p}}{\partial n}-if\underbrace{\left(u-\frac{v}{i}\right)}_{\text{since }\frac{1}{i}=-i\,,\,u-\frac{v}{i}=u+iv=\tilde{u}}+K_V\frac{\partial^2\tilde{u}}{\partial z^2}=0$$

Finally, the complete second order differential equation is:

$$\boxed{K_V\frac{\partial^2\tilde{u}}{\partial z^2}-if\tilde{u}=\frac{1}{\rho_0}\frac{\partial\tilde{p}}{\partial n}} \tag{A.6}$$

Boundary conditions:

No-slip condition at the bottom: $(\tilde{u})_{z=-h}=0$

At the surface: $K_V\left(\frac{\partial\tilde{u}}{\partial z}\right)_{z=0}=\frac{1}{\rho_0}\tilde{\tau}^s$

Equation A.6 is a non-homogenous, second order differential equation with constant coefficients. The total solution will be the sum of the homogenous with the particular solution: $s_T(z) = s_H(z) + s_P(z)$.

The first step is to derive the homogenous part of the solution $s_H(z)$.

$$a\overset{''}{s_H}(z) + b\overset{'}{s_H}(z) + cs_H(z) = 0 \quad \text{where} \quad a = K_V \ , \ b = 0 \text{ and } c = -if \tag{A.7}$$

Writing the characteristic equation and solving the second degree equation provides two roots:

$$m_1 = \frac{-b + \sqrt{b^2 - 4ac}}{2a} = \frac{\sqrt{-4K_V\left(-if\right)}}{2K_V} = \sqrt{\frac{if}{K_V}} \tag{A.8a}$$

$$m_2 = \frac{-b - \sqrt{b^2 - 4ac}}{2a} = \frac{-\sqrt{-4K_V\left(-if\right)}}{2K_V} = -\sqrt{\frac{if}{K_V}} \tag{A.8b}$$

With two distinct roots, even if they are complex, the general form of the solution is:

$$s_H(z) = C_1 e^{m_1 z} + C_2 e^{m_2 z} \Leftrightarrow s_H(z) = C_1 e^{\sqrt{\frac{if}{K_V}} z} + C_2 e^{-\sqrt{\frac{if}{K_V}} z} \tag{A.9}$$

The particular solution is a constant A, since the forcing function of the differential equation is a constant too:

$$s_P(z) = A \Rightarrow \overset{'}{s_P}(z) = 0 \Rightarrow \overset{''}{s_P}(z) = 0 \tag{A.10}$$

Plugging **Equation A.10** into **Equation A.6**:

$$K_V \times 0 - ifA = \frac{1}{\rho_0}\frac{\partial \tilde{p}}{\partial n} \Rightarrow A = -\frac{1}{i\rho_0 f}\frac{\partial \tilde{p}}{\partial n} \Rightarrow A = \frac{i}{\rho_0 f}\frac{\partial \tilde{p}}{\partial n} \tag{A.11}$$

Without applying boundary conditions, the general solution $s_T(z) \equiv \tilde{u}\left(z\right)$:

$$\tilde{u}\left(z\right) = C_1 e^{\sqrt{\frac{if}{K_V}} z} + C_2 e^{-\sqrt{\frac{if}{K_V}} z} + \frac{i}{\rho_0 f}\frac{\partial \tilde{p}}{\partial n} \tag{A.12}$$

Applying the no-slip boundary condition:

$$C_1 e^{-\sqrt{\frac{if}{K_V}} h} + C_2 e^{\sqrt{\frac{if}{K_V}} h} + \frac{i}{\rho_0 f}\frac{\partial \tilde{p}}{\partial n} = 0 \tag{A.13}$$

Differentiation of the general solution is needed before applying the surface boundary condition:

$$\begin{aligned}\frac{\partial \tilde{u}}{\partial z} &= \frac{\partial}{\partial z}\left(C_1 e^{\sqrt{\frac{if}{K_V}} z} + C_2 e^{-\sqrt{\frac{if}{K_V}} z} + \frac{i}{\rho_0 f}\frac{\partial \tilde{p}}{\partial n}\right) = C_1 \frac{\partial}{\partial z}\left(e^{\sqrt{\frac{if}{K_V}} z}\right) + C_2 \frac{\partial}{\partial z}\left(e^{-\sqrt{\frac{if}{K_V}} z}\right) = \\ &= C_1 \sqrt{\frac{if}{K_V}} e^{\sqrt{\frac{if}{K_V}} z} + C_2 \left(-\sqrt{\frac{if}{K_V}}\right) e^{-\sqrt{\frac{if}{K_V}} z} = \\ &= C_1 \sqrt{\frac{if}{K_V}} e^{\sqrt{\frac{if}{K_V}} z} - C_2 \sqrt{\frac{if}{K_V}} e^{-\sqrt{\frac{if}{K_V}} z}\end{aligned} \tag{A.14}$$

Using this result:

$$K_V\left(\frac{\partial\tilde{u}}{\partial z}\right)_{z=0}=\frac{1}{\rho_0}\tilde{\tau}^s\Leftrightarrow K_V\left(C_1\sqrt{\frac{if}{K_V}}-C_2\sqrt{\frac{if}{K_V}}\right)=\frac{\tilde{\tau}^s}{\rho_0}\Leftrightarrow\sqrt{\frac{if}{K_V}}\left(C_1-C_2\right)=\frac{\tilde{\tau}^s}{\rho_0K_V}$$
$$\Leftrightarrow C_1-C_2=\frac{\tilde{\tau}^s}{\rho_0K_V\sqrt{\frac{if}{K_V}}}=\frac{\tilde{\tau}^s}{\rho_0\sqrt{ifK_V}} \tag{A.15}$$

At this point, it is convenient to introduce the Ekman depth:

$$D=\pi\sqrt{\frac{2K_V}{|f|}}\Leftrightarrow\sqrt{K_V}=\frac{D\sqrt{|f|}}{\pi\sqrt{2}} \tag{A.16}$$

Equation A.15 can be rewritten as:

$$\begin{aligned}C_1-C_2&=\frac{\tilde{\tau}^s}{\rho_0\sqrt{ifK_V}}=\frac{\tilde{\tau}^s}{\rho_0\sqrt{i}\sqrt{f}\sqrt{K_V}}=\frac{\tilde{\tau}^s}{\rho_0\frac{\sqrt{2}}{2}\left(1+i\right)\frac{D\sqrt{|f|}}{\pi\sqrt{2}}\sqrt{f}}\\&=\frac{\tilde{\tau}^s}{\rho_0\left(\frac{1}{2}+\frac{1}{2}i\right)\frac{D\sqrt{|f|}}{\pi}\sqrt{f}}=\left(1-i\right)\frac{\pi\tilde{\tau}^s}{\rho_0\sqrt{f|f|}D}=\left(1-i\right)\frac{\pi\tilde{\tau}^s}{\rho_0\sqrt{\frac{f^2}{\lambda}}D}\\&=\left(1-i\right)\frac{\pi\tilde{\tau}^s}{\rho_0\sqrt{f^2}\sqrt{\frac{1}{\lambda}}D}=\frac{\left(1-i\right)}{\sqrt{\frac{1}{\lambda}}}\frac{\pi\tilde{\tau}^s}{\rho_0|f|D}=\sqrt{\lambda}\left(1-i\right)\frac{\pi\tilde{\tau}^s}{\rho_0|f|D}\end{aligned}$$

Noting that $\sqrt{\lambda}\left(1-i\right)=1-\lambda i$ when $\lambda\neq0$, the last equation becomes:

$$C_1-C_2=\left(1-\lambda i\right)\frac{\pi\tilde{\tau}^s}{\rho_0|f|D} \tag{A.17}$$

In the Estrade et al. (2008) article, the right hand side of the last equation is denoted as $\tilde{u}_0$, which is the surface Ekman velocity in the deep ocean limit.

$$\boxed{\tilde{u}_0=\left(1-\lambda i\right)\frac{\pi\tilde{\tau}^s}{\rho_0|f|D}} \tag{A.18}$$

Expressing C_1 as a function of C_2 using **Equation A.17** and substituting this result in **Equation A.13**:

$$\left(C_2-\tilde{u}_0\right)e^{-\sqrt{\frac{if}{K_V}}h}+C_2e^{\sqrt{\frac{if}{K_V}}h}+\frac{i}{\rho_0f}\frac{\partial\tilde{p}}{\partial n}=0\Leftrightarrow C_2e^{-\sqrt{\frac{if}{K_V}}h}+\tilde{u}_0e^{-\sqrt{\frac{if}{K_V}}h}+C_2e^{\sqrt{\frac{if}{K_V}}h}+\frac{i}{\rho_0f}\frac{\partial\tilde{p}}{\partial n}=0$$

$$C_2\underbrace{\left(e^{-\sqrt{\frac{if}{K_V}}h}+e^{\sqrt{\frac{if}{K_V}}h}\right)}_{\text{remembering that }\cosh x=\frac{e^x+e^{-x}}{2}}+\tilde{u}_0e^{-\sqrt{\frac{if}{K_V}}h}+\frac{i}{\rho_0f}\frac{\partial\tilde{p}}{\partial n}=0$$

$$C_2=-\frac{\tilde{u}_0e^{-\sqrt{\frac{if}{K_V}}h}+\frac{i}{\rho_0f}\frac{\partial\tilde{p}}{\partial n}}{2\cosh\left(\sqrt{\frac{if}{K_V}}h\right)} \tag{A.19}$$

Going back to **Equation A.17**:

$$C_1 + \frac{\tilde{u}_0 e^{-\sqrt{\frac{if}{K_V}}h} + \frac{i}{\rho_0 f}\frac{\partial \tilde{p}}{\partial n}}{2\cosh\left(\sqrt{\frac{if}{K_V}}h\right)} = \tilde{u}_0 \Leftrightarrow C_1 = \frac{2\tilde{u}_0 \cosh\left(\sqrt{\frac{if}{K_V}}\right)}{2\cosh\left(\sqrt{\frac{if}{K_V}}h\right)} - \frac{\tilde{u}_0 e^{-\sqrt{\frac{if}{K_V}}h} + \frac{i}{\rho_0 f}\frac{\partial \tilde{p}}{\partial n}}{2\cosh\left(\sqrt{\frac{if}{K_V}}h\right)}$$

$$C_1 = \frac{\tilde{u}_0\left(e^{-\sqrt{\frac{if}{K_V}}h} + e^{\sqrt{\frac{if}{K_V}}h}\right) - \tilde{u}_0 e^{-\sqrt{\frac{if}{K_V}}h} - \frac{i}{\rho_0 f}\frac{\partial \tilde{p}}{\partial n}}{2\cosh\left(\sqrt{\frac{if}{K_V}}h\right)}$$

$$C_1 = \frac{\tilde{u}_0 e^{\sqrt{\frac{if}{K_V}}h} - \frac{i}{\rho_0 f}\frac{\partial \tilde{p}}{\partial n}}{2\cosh\left(\sqrt{\frac{if}{K_V}}h\right)} \tag{A.20}$$

Plugging the constants into **Equation A.12**:

$$\tilde{u} = \left(\frac{\tilde{u}_0 e^{\sqrt{\frac{if}{K_V}}h} - \frac{i}{\rho_0 f}\frac{\partial \tilde{p}}{\partial n}}{2\cosh\left(\sqrt{\frac{if}{K_V}}h\right)}\right) e^{\sqrt{\frac{if}{K_V}}z} + \left(-\frac{\tilde{u}_0 e^{-\sqrt{\frac{if}{K_V}}h} + \frac{i}{\rho_0 f}\frac{\partial \tilde{p}}{\partial n}}{2\cosh\left(\sqrt{\frac{if}{K_V}}h\right)}\right) e^{-\sqrt{\frac{if}{K_V}}z} + \frac{i}{\rho_0 f}\frac{\partial \tilde{p}}{\partial n}$$

$$\tilde{u} = \frac{\tilde{u}_0 e^{\sqrt{\frac{if}{K_V}}h} e^{\sqrt{\frac{if}{K_V}}z} - \frac{i}{\rho_0 f}\frac{\partial \tilde{p}}{\partial n} e^{\sqrt{\frac{if}{K_V}}z} - \tilde{u}_0 e^{-\sqrt{\frac{if}{K_V}}h} e^{-\sqrt{\frac{if}{K_V}}z} - \frac{i}{\rho_0 f}\frac{\partial \tilde{p}}{\partial n} e^{-\sqrt{\frac{if}{K_V}}z} + \left(e^{-\sqrt{\frac{if}{K_V}}h} + e^{\sqrt{\frac{if}{K_V}}h}\right)\frac{i}{\rho_0 f}\frac{\partial \tilde{p}}{\partial n}}{2\cosh\left(\sqrt{\frac{if}{K_V}}h\right)}$$

$$\tilde{u} = \frac{\tilde{u}_0 e^{\sqrt{\frac{if}{K_V}}(z+h)} - \tilde{u}_0 e^{-\sqrt{\frac{if}{K_V}}(z+h)} + \frac{i}{\rho_0 f}\frac{\partial \tilde{p}}{\partial n}\left(-e^{\sqrt{\frac{if}{K_V}}z} - e^{-\sqrt{\frac{if}{K_V}}z} + e^{-\sqrt{\frac{if}{K_V}}h} + e^{\sqrt{\frac{if}{K_V}}h}\right)}{2\cosh\left(\sqrt{\frac{if}{K_V}}h\right)}$$

$$\tilde{u} = \frac{2\tilde{u}_0 \sinh\left[\sqrt{\frac{if}{K_V}}(z+h)\right] - \frac{i}{\rho_0 f}\frac{\partial \tilde{p}}{\partial n}\left(e^{\sqrt{\frac{if}{K_V}}z} + e^{-\sqrt{\frac{if}{K_V}}z}\right) + \frac{i}{\rho_0 f}\frac{\partial \tilde{p}}{\partial n}\left(e^{\sqrt{\frac{if}{K_V}}h} + e^{-\sqrt{\frac{if}{K_V}}h}\right)}{2\cosh\left(\sqrt{\frac{if}{K_V}}h\right)}$$

$$\tilde{u} = \tilde{u}_0 \frac{\sinh\left[\sqrt{\frac{if}{K_V}}(z+h)\right]}{\cosh\left[\sqrt{\frac{if}{K_V}}h\right]} + \frac{-\frac{2i}{\rho_0 f}\frac{\partial \tilde{p}}{\partial n}\cosh\left[\sqrt{\frac{if}{K_V}}z\right] + \frac{2i}{\rho_0 f}\frac{\partial \tilde{p}}{\partial n}\cosh\left[\sqrt{\frac{if}{K_V}}h\right]}{2\cosh\left[\sqrt{\frac{if}{K_V}}h\right]}$$

$$\tilde{u} = \tilde{u}_0 \frac{\sinh\left[\sqrt{\frac{if}{K_V}}(z+h)\right]}{\cosh\left[\sqrt{\frac{if}{K_V}}h\right]} - \frac{i}{\rho_0 f}\frac{\partial \tilde{p}}{\partial n}\left(\frac{\cosh\left[\sqrt{\frac{if}{K_V}}z\right]}{\cosh\left[\sqrt{\frac{if}{K_V}}h\right]} - 1\right) \tag{A.21}$$

The complex pressure gradient can be transformed into a complex geostrophic velocity:

$$\frac{i}{\rho_0 f}\frac{\partial \tilde{p}}{\partial n} = \frac{i}{\rho_0 f}\left(\frac{\partial p}{\partial x} + i\frac{\partial p}{\partial y}\right) = \frac{i}{\rho_0 f}\frac{\partial p}{\partial x} + \frac{i^2}{\rho_0 f}\frac{\partial p}{\partial y} = \underbrace{-\frac{1}{\rho_0 f}\frac{\partial p}{\partial y}}_{=u_g} + i\underbrace{\frac{1}{\rho_0 f}\frac{\partial p}{\partial x}}_{=v_g} = u_g + iv_g = \tilde{u}_g \tag{A.22}$$

While $\sqrt{\frac{if}{K_V}}$ can be simplified as follows:

$$\sqrt{\frac{if}{K_V}} = \sqrt{i}\frac{\sqrt{f}}{\sqrt{K_V}} = \pm\frac{\sqrt{2}}{2}(1+i)\frac{\sqrt{f}}{\frac{\sqrt{|f|}D}{\pi\sqrt{2}}} = \pm\sqrt{\lambda}(1+i)\frac{\pi}{D} \tag{A.23}$$

Noting that $\lambda = \pm 1$ and

$$\sqrt{\pm 1} = \frac{1+i}{2} \pm \frac{1-i}{2} \tag{A.24}$$

leads to:

$$\sqrt{\pm 1}(1+i) = \left(\frac{1+i}{2} \pm \frac{1-i}{2}\right)(1+i) = i \pm 1 = \pm 1 \left(\frac{i}{\pm 1} + 1\right) = \lambda(1+i\lambda) \tag{A.25}$$

Above, the particularity $1/\lambda = \lambda$ was used. Going back to **Equation A.23**, knowing that $\lambda^2 = 1$, and naming the expression as c gives:

$$c = (\pm 1)\lambda(1+i\lambda)\frac{\pi}{D} = \lambda^2(1+i\lambda)\frac{\pi}{D} = (1+i\lambda)\,\frac{\pi}{D} \Rightarrow \boxed{c = (1+i\lambda)\frac{\pi}{D}} \tag{A.26}$$

Taking all these simplifications into account:

$$\boxed{\tilde{u} = \tilde{u}_0 \frac{\sinh[c(z+h)]}{\cosh[ch]} + \tilde{u}_g \left(1 - \frac{\cosh[cz]}{\cosh[ch]}\right)} \tag{A.27}$$

Dividing the flow into Ekman and geostrophic components:

$$\tilde{u} = u + iv = (u_E + u_g) + i\,(v_E + v_g) = (u_E + iv_E) + (u_g + iv_g) = \tilde{u}_E + \tilde{u}_g \tag{A.28}$$

The Ekman component of the flow is:

$$\tilde{u} = \underbrace{\tilde{u}_0 \frac{\sinh[c(z+h)]}{\cosh[ch]} - \tilde{u}_g \frac{\cosh[cz]}{\cosh[ch]}}_{=\tilde{u}_E} + \tilde{u}_g \Rightarrow \boxed{\tilde{u}_E = \tilde{u}_0 \frac{\sinh[c(z+h)]}{\cosh[ch]} - \tilde{u}_g \frac{\cosh[cz]}{\cosh[ch]}} \tag{A.29}$$

A.2 Horizontally-varying structure functions, Ekman transport and meridional geostrophic velocity

The full Ekman transport accounts for both bottom and top layers, hence it is integrated for the whole water column:

$$\widetilde{U}_E = \int_{z=-h}^{z=0} \tilde{u}_E \, dz = \tilde{u}_0 \int_{z=-h}^{z=0} \frac{\sinh[c(z+h)]}{\cosh[ch]} \, dz - \int_{z=-h}^{z=0} \tilde{u}_g \frac{\cosh[cz]}{\cosh[ch]} \, dz \tag{A.30}$$

Solving the first integral using $t = c\,(z+h) \Rightarrow \frac{dt}{dz} = c \Rightarrow dz = \frac{1}{c} dt$ as a substitution:

$$\int \frac{\sinh[c(z+h)]}{\cosh[ch]} \, dz = \frac{1}{c\cosh[ch]} \int \sinh t \, dt = \frac{1}{c\cosh[ch]} \left(\cosh t + A_1\right) = \frac{\cosh[c\,(z+h)]}{c\cosh[ch]} + A_2 \tag{A.31}$$

Evaluating the result at the integral's limits:

$$\left(\frac{\cosh[c\,(z+h)]}{c\cosh[ch]} + A_2\right)_{z=0} - \left(\frac{\cosh[c\,(z+h)]}{c\cosh[ch]} + A_2\right)_{z=-h} = \frac{\cosh[ch] - 1}{c\cosh[ch]} \tag{A.32}$$

Solving the second integral using $s = cz \Rightarrow \frac{ds}{dz} = c \Rightarrow dz = \frac{1}{c} ds$ as a substitution:

$$\int \frac{\cosh[cz]}{\cosh[ch]} dz = \frac{1}{c\cosh[ch]} \int \cosh s \, ds = \frac{1}{c\cosh[ch]} \left(\sinh t + A_3\right) = \frac{\sinh[cz]}{c\cosh[ch]} + A_4 \tag{A.33}$$

Evaluating the result at the integral's limits:

$$\left(\frac{\sinh[cz]}{c\cosh[ch]} + A_4\right)_{z=0} - \left(\frac{\sinh[cz]}{c\cosh[ch]} + A_4\right)_{z=-h} = \frac{\sinh[ch]}{c\cosh[ch]} \tag{A.34}$$

Going back to **Equation A.30**:

$$\begin{aligned}
\widetilde{U}_E &= \frac{\tilde{u}_0}{c}\left(\frac{\cosh[ch]-1}{\cosh[ch]}\right) - \tilde{u}_g\left(\frac{\sinh[ch]}{c\cosh[ch]}\right) = \frac{(1-\lambda i)\,\frac{\pi\tilde{\tau}^s}{\rho_0|\tilde{f}|D}}{(1+\lambda i)\,\frac{\pi}{D}}\left(\frac{\cosh[ch]-1}{\cosh[ch]}\right) - \frac{(u_g+iv_g)}{(1+\lambda i)\,\frac{\pi}{D}}\left(\frac{\sinh[ch]}{\cosh[ch]}\right) \\
&= (-i\lambda)\frac{\tau_x+i\tau_y}{\rho_0\underbrace{|f|}_{=\lambda f}}\left(\frac{\cosh\left[(1+\lambda i)\,\frac{\pi}{D}h\right]-1}{\cosh\left[(1+\lambda i)\,\frac{\pi}{D}h\right]}\right) - \frac{D}{\pi}\left[\left(\frac{1}{2}-\frac{1}{2}i\lambda\right)(u_g+iv_g)\right]\left(\frac{\sinh\left[\frac{\pi}{D}h+\lambda i\frac{\pi}{D}h\right]}{\cosh\left[\frac{\pi}{D}h+\lambda i\frac{\pi}{D}h\right]}\right) \\
&= \frac{\tau_y - i\tau_x}{\rho_0 f}\left(\frac{\cosh\left[(1+\lambda i)\,\frac{\pi}{D}h\right]-1}{\cosh\left[(1+\lambda i)\,\frac{\pi}{D}h\right]}\right) - \frac{D}{2\pi}\left[(u_g+\lambda v_g)+i\,(v_g-\lambda u_g)\right]\left(\frac{\sinh\left[\frac{\pi}{D}h+\lambda i\frac{\pi}{D}h\right]}{\cosh\left[\frac{\pi}{D}h+\lambda i\frac{\pi}{D}h\right]}\right)
\end{aligned} \tag{A.35}$$

At this point it is nice to remember that:

$$\sinh(x+iy) = \sinh(x)\cos(y) + i\cosh(x)\sin(y) \tag{A.36a}$$

$$\cosh(x+iy) = \cosh(x)\cos(y) + i\sinh(x)\sin(y) \tag{A.36b}$$

Using **Equation A.35**:

$$\widetilde{U}_E = \frac{\tau_y - i\tau_x}{\rho_0 f}\left(\frac{\cosh\left[\frac{\pi}{D}h\right]\cos\left[\lambda\frac{\pi}{D}h\right] + i\sinh\left[\frac{\pi}{D}h\right]\sin\left[\lambda\frac{\pi}{D}h\right] - 1}{\cosh\left[\frac{\pi}{D}h\right]\cos\left[\lambda\frac{\pi}{D}h\right] + i\sinh\left[\frac{\pi}{D}h\right]\sin\left[\lambda\frac{\pi}{D}h\right]}\right)$$

$$- \frac{D}{2\pi}\left[\underbrace{\left(u_g + \lambda v_g\right)}_{=t_1} + i\underbrace{\left(v_g - \lambda u_g\right)}_{=t_2}\right]\left(\frac{\sinh\left[\frac{\pi}{D}h\right]\cos\left[\lambda\frac{\pi}{D}h\right] + i\cosh\left[\frac{\pi}{D}h\right]\sin\left[\lambda\frac{\pi}{D}h\right]}{\cosh\left[\frac{\pi}{D}h\right]\cos\left[\lambda\frac{\pi}{D}h\right] + i\sinh\left[\frac{\pi}{D}h\right]\sin\left[\lambda\frac{\pi}{D}h\right]}\right)$$

Since $\lambda = \pm 1$, then $\cos(\lambda x) = \cos x$ and $\sin^2(\lambda x) = \sin x$, which means that some simplifications can be made:

$$\frac{1}{\rho_0 f}\frac{\tau_y\cosh\left[\frac{\pi}{D}h\right]\cos\left[\frac{\pi}{D}h\right] - \tau_y + \tau_x\sinh\left[\frac{\pi}{D}h\right]\sin\left[\lambda\frac{\pi}{D}h\right] + i\left(\tau_y\sinh\left[\frac{\pi}{D}h\right]\sin\left[\lambda\frac{\pi}{D}h\right] - \tau_x\cosh\left[\frac{\pi}{D}h\right]\cos\left[\frac{\pi}{D}h\right] + \tau_x\right)}{\cosh\left[\frac{\pi}{D}h\right]\cos\left[\frac{\pi}{D}h\right] + i\sinh\left[\frac{\pi}{D}h\right]\sin\left[\lambda\frac{\pi}{D}h\right]}$$

$$- \frac{D}{2\pi}\frac{t_1\sinh\left[\frac{\pi}{D}h\right]\cos\left[\frac{\pi}{D}h\right] - t_2\cosh\left[\frac{\pi}{D}h\right]\sin\left[\lambda\frac{\pi}{D}h\right] + i\left(t_1\cosh\left[\frac{\pi}{D}h\right]\sin\left[\lambda\frac{\pi}{D}h\right] + t_2\sinh\left[\frac{\pi}{D}h\right]\cos\left[\frac{\pi}{D}h\right]\right)}{\cosh\left[\frac{\pi}{D}h\right]\cos\left[\frac{\pi}{D}h\right] + i\sinh\left[\frac{\pi}{D}h\right]\sin\left[\lambda\frac{\pi}{D}h\right]} \tag{A.37}$$

Let

$$j = \tau_y\cosh\left[\frac{\pi}{D}h\right]\cos\left[\frac{\pi}{D}h\right] - \tau_y + \tau_x\sinh\left[\frac{\pi}{D}h\right]\sin\left[\lambda\frac{\pi}{D}h\right] \tag{A.38a}$$

$$k = \tau_y\sinh\left[\frac{\pi}{D}h\right]\sin\left[\lambda\frac{\pi}{D}h\right] - \tau_x\cosh\left[\frac{\pi}{D}h\right]\cos\left[\frac{\pi}{D}h\right] + \tau_x \tag{A.38b}$$

$$l = \cosh\left[\frac{\pi}{D}h\right]\cos\left[\frac{\pi}{D}h\right] \tag{A.38c}$$

$$m = \sinh\left[\frac{\pi}{D}h\right]\sin\left[\lambda\frac{\pi}{D}h\right] \tag{A.38d}$$

$$n = t_1\sinh\left[\frac{\pi}{D}h\right]\cos\left[\frac{\pi}{D}h\right] - t_2\cosh\left[\frac{\pi}{D}h\right]\sin\left[\lambda\frac{\pi}{D}h\right] \tag{A.38e}$$

$$o = t_1\cosh\left[\frac{\pi}{D}h\right]\sin\left[\lambda\frac{\pi}{D}h\right] + t_2\sinh\left[\frac{\pi}{D}h\right]\cos\left[\frac{\pi}{D}h\right] \tag{A.38f}$$

$$p = l = \cosh\left[\frac{\pi}{D}h\right]\cos\left[\frac{\pi}{D}h\right] \tag{A.38g}$$

$$q = m = \sinh\left[\frac{\pi}{D}h\right]\sin\left[\lambda\frac{\pi}{D}h\right] \tag{A.38h}$$

Rewriting everything:

$$\tilde{U}_E = \frac{1}{\rho_0 f}\left[\frac{j+ik}{l+im}\right] - \frac{D}{2\pi}\left[\frac{n+io}{p+iq}\right] = \frac{1}{\rho_0 f}\left[\frac{jl+km}{l^2+m^2} + i\frac{kl-jm}{l^2+m^2}\right] - \frac{D}{2\pi}\left[\frac{np+oq}{p^2+q^2} + i\frac{op-nq}{p^2+q^2}\right] \tag{A.39}$$

Since only the zonal component of the Ekman transport is important:

$$\mathfrak{Re}\left\{\widetilde{U}_E\right\} = U_E = \frac{1}{\rho_0 f}\left[\frac{jl+km}{l^2+m^2}\right] - \frac{D}{2\pi}\left[\frac{np+oq}{p^2+q^2}\right] \tag{A.40}$$

After some algebra work:

$$U_E = \frac{1}{\rho_0 f}\left[\frac{\tau_y\left(\sinh\left[\frac{\pi}{D}h\right]\sin\left[\lambda\frac{\pi}{D}h\right]\right)^2+\tau_y\left(\cosh\left[\frac{\pi}{D}h\right]\cos\left[\frac{\pi}{D}h\right]\right)^2-\tau_y\cosh\left[\frac{\pi}{D}h\right]\cos\left[\frac{\pi}{D}h\right]+\tau_x\sinh\left[\frac{\pi}{D}h\right]\sin\left[\lambda\frac{\pi}{D}h\right]}{\left(\cosh\left[\frac{\pi}{D}h\right]\cos\left[\frac{\pi}{D}h\right]\right)^2+\left(\sinh\left[\frac{\pi}{D}h\right]\sin\left[\lambda\frac{\pi}{D}h\right]\right)^2}\right]$$

$$-\frac{D}{2\pi}\left[\frac{t_1\sinh\left[\frac{\pi}{D}h\right]\cosh\left[\frac{\pi}{D}h\right]\cos^2\left[\frac{\pi}{D}h\right]-t_2\sin\left[\lambda\frac{\pi}{D}h\right]\cos\left[\frac{\pi}{D}h\right]\cosh^2\left[\frac{\pi}{D}h\right]+t_1\cosh\left[\frac{\pi}{D}h\right]\sinh\left[\frac{\pi}{D}h\right]\sin^2\left[\frac{\pi}{D}h\right]+t_2\sin\left[\lambda\frac{\pi}{D}h\right]\cos\left[\frac{\pi}{D}h\right]\sinh^2\left[\frac{\pi}{D}h\right]}{\left(\cosh\left[\frac{\pi}{D}h\right]\cos\left[\frac{\pi}{D}h\right]\right)^2+\left(\sinh\left[\frac{\pi}{D}h\right]\sin\left[\lambda\frac{\pi}{D}h\right]\right)^2}\right]$$

Defining the horizontally-varying structure functions as:

$$\boxed{\alpha = \left(\cosh\left[\frac{\pi}{D}h\right]\cos\left[\frac{\pi}{D}h\right]\right)^2 + \left(\sinh\left[\frac{\pi}{D}h\right]\sin\left[\frac{\pi}{D}h\right]\right)^2} \tag{A.41a}$$

$$\boxed{S_1 = \cosh\left[\frac{\pi}{D}h\right]\cos\left[\frac{\pi}{D}h\right]\alpha^{-1}} \tag{A.41b}$$

$$\boxed{S_2 = \sinh\left[\frac{\pi}{D}h\right]\sin\left[\lambda\frac{\pi}{D}h\right]\alpha^{-1}} \tag{A.41c}$$

$$\boxed{T_1 = \cosh\left[\frac{\pi}{D}h\right]\sinh\left[\frac{\pi}{D}h\right]\alpha^{-1}} \tag{A.41d}$$

$$\boxed{T_2 = \cos\left[\frac{\pi}{D}h\right]\sin\left[\lambda\frac{\pi}{D}h\right]\alpha^{-1}} \tag{A.41e}$$

The expression for the total (zonal) Ekman transport becomes:

$$\frac{1}{\rho_0 f}\left(\frac{\tau_y\alpha}{\alpha} - \tau_y S_1 + \tau_x S_2\right) - \frac{D}{2\pi}\left(t_1T_1\cos^2\left[\frac{\pi}{D}h\right] - t_2T_2\cosh^2\left[\frac{\pi}{D}h\right] + t_1T_1\sin^2\left[\lambda\frac{\pi}{D}h\right] + t_2T_2\sinh^2\left[\frac{\pi}{D}h\right]\right) =$$

$$= (1-S_1)\frac{\tau_y}{\rho_0 f} + S_2\frac{\tau_x}{\rho_0 f} - \frac{D}{2\pi}\left\{t_1T_1\underbrace{\left(\cos^2\left[\frac{\pi}{D}h\right] + \sin^2\left[\frac{\pi}{D}h\right]\right)}_{=1} + t_2T_2\underbrace{\left(-\cosh^2\left[\frac{\pi}{D}h\right] + \sinh^2\left[\frac{\pi}{D}h\right]\right)}_{=-1}\right\}$$

$$= (1-S_1)\frac{\tau_y}{\rho_0 f} + S_2\frac{\tau_x}{\rho_0 f} - \frac{D}{2\pi}\left[t_1T_1 - t_2T_2\right] = (1-S_1)\frac{\tau_y}{\rho_0 f} + S_2\frac{\tau_x}{\rho_0 f} - \frac{D}{2\pi}\left[\left(u_g + \lambda v_g\right)T_1 - \left(v_g - \lambda u_g\right)T_2\right]$$

Finally,

$$\boxed{U_E = (1-S_1)\frac{\tau_y}{\rho_0 f} + S_2\frac{\tau_x}{\rho_0 f} - \frac{D}{2\pi}\left[\left(\lambda T_1 - T_2\right)v_g + \left(T_1 + \lambda T_2\right)u_g\right]} \tag{A.43}$$

Since the total cross-shore transport must be zero everywhere, another relation can be obtained. Assuming geostrophic barotropic flow (u_g is independent of depth):

$$U_T = 0 \Leftrightarrow \int_{z=-h}^{z=0}\left(u_E + u_g\right)dz = 0 \Leftrightarrow \int_{z=-h}^{z=0} u_E\,dz + u_g\int_{z=-h}^{z=0} dz = 0$$

$$\Leftrightarrow U_E + u_g\left[0 - (-h)\right] = 0 \Rightarrow \boxed{U_E = -u_g h} \tag{A.44}$$

Combining **Equations A.43** and **A.44** to eliminate U_E and solving for v_g gives:

$$\boxed{v_g = \frac{2\pi}{\rho_0 f D}\left[\frac{1-S_1}{\lambda T_1 - T_2}\tau_y + \frac{S_2}{\lambda T_1 - T_2}\tau_x\right] - u_g\frac{T_1 + \lambda T_2 - 2\pi h/D}{\lambda T_1 - T_2}} \tag{A.45}$$

A.3 Stream function

Using the formal definition for a stream function:

$$\begin{cases} w = \frac{\partial \psi}{\partial x} \\ u = -\frac{\partial \psi}{\partial z} \end{cases} \tag{A.46}$$

Integrating in the z direction and substituting the total velocity for the Ekman and geostrophic components gives:

$$-\int_{\psi(x,z)}^{\psi(x,0)} d\psi = \int_z^0 u dz = \int_z^0 (u_E + u_g)\, dz \Rightarrow \psi(x,z) - \psi(x,0) = \int_z^0 u_E\, dz + \int_z^0 u_g\, dz \tag{A.47}$$

Assuming $\psi(x,0) = 0$ and knowing that the surface Ekman transport is given by $\widetilde{U}_E^s = \int_z^0 \tilde{u}_E dz$ with $\tilde{u}_E = u_E + iv_E$ gives:

$$\boxed{\psi(x,z) = \mathfrak{Re}\left\{\widetilde{U}_E^s\right\} - u_g z} \tag{A.48}$$

In **Equation A.30** the integration was done for the whole water column. If the integral's limits where changed to z and 0, the surface Ekman transport $\widetilde{U}_E^s$ would have been obtained. The result is:

$$\widetilde{U}_E^s = \frac{1}{c}\left[\tilde{u}_0\left(1 - \frac{\cosh[c(z+h)]}{\cosh[ch]}\right) + \tilde{u}_g\frac{\sinh[cz]}{\sinh[ch]}\right] \tag{A.49}$$

Alternatively:

$$\boxed{\psi(x,z) = \mathfrak{Re}\left\{\frac{1}{c}\left[\tilde{u}_0\left(1 - \frac{\cosh[c(z+h)]}{\cosh[ch]}\right) + \tilde{u}_g\frac{\sinh[cz]}{\sinh[ch]}\right]\right\} - u_g z} \tag{A.50}$$

Appendix B

Parameter calculation

SOUTH LOCATION	NORTH LOCATION
$K_V = 0.01\,\mathrm{m\,s^{-2}}$	$K_V = 0.01\,\mathrm{m\,s^{-2}}$
$f = 0.890 \times 10^{-4}\,\mathrm{s^{-1}}$	$f = 0.945 \times 10^{-4}\,\mathrm{s^{-1}}$
$D = \pi\sqrt{2K_V/\lvert f\rvert} = 47.01\,\mathrm{m}$	$D = \pi\sqrt{2K_V/\lvert f\rvert} = 45.60\,\mathrm{m}$
$K_H = 100\,\mathrm{m\,s^{-2}}$	$K_H = 100\,\mathrm{m\,s^{-2}}$
$L_E = \pi\sqrt{2K_H/\lvert f\rvert} = 4701.5\,\mathrm{m}$	$L_E = \pi\sqrt{2K_H/\lvert f\rvert} = 4565.5\,\mathrm{m}$
$S = 300/22000 = 0.0136$	$S = 125/55000 = 0.00227$
$0.75D/S = 2592.5\,\mathrm{m}$	$0.75D/S = 15\,066\,\mathrm{m}$
$L_U = \max\left[2592.5\ ;\ 4705.5\right] = 4701.5\,\mathrm{m}$	$L_U = \max\left[4565.5\ ;\ 15066\right] = 15\,066\,\mathrm{m}$

Calculating the slope S is simple as it only requires inspection of the bathymetry profile. For the South location, the depth goes from 0 to $300\,\mathrm{m}$ in $22\,\mathrm{km}$, while for the North location it goes from 0 to $125\,\mathrm{m}$ in $55\,\mathrm{km}$. Regarding the Ekman depth, since it is practically the same for both locations, a single value of $D = 46\,\mathrm{m}$ will be used.